University of Ulm
Faculty of
Natural Sciences

Diplom Thesis

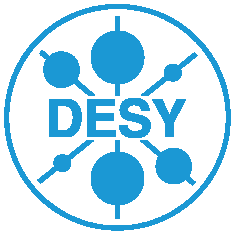

Search for Point Sources of High-Energy Neutrinos with the AMANDA Detector

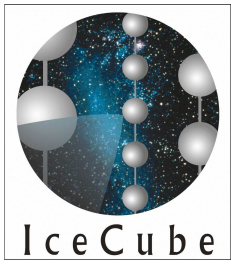

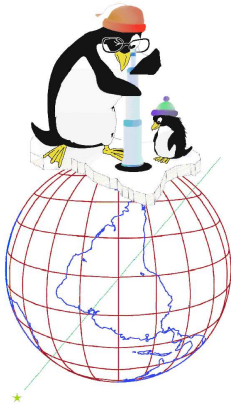

prepared at
DESY Zeuthen

by Rafael Florian Lang
September 2005

Referees: Prof. Dr. Frank Steiner
and Prof. Dr. Hartmut Jex

Contents

Chapter 1

Overview

1.1 High Energy Astroparticle Physics

The field of high energy astroparticle physics is flourishing. Many experiments around the world help to solve long standing mysteries, and exciting discoveries are either being made or are just around the corner. Part I of this thesis is about these mysteries and ways to clarify them using neutrinos. It is about the peculiarities of neutrinos and about the largest detector in the world with which one detects them: about AMANDA, the Antarctic Muon and Neutrino Detector Array. Thus in this thesis the term *high energy* will denote energies above $\approx 100\,\mathrm{GeV}$, roughly corresponding to the muon threshold of the AMANDA detector.

Organization of Part I

Chapter 2, *Cosmic Messengers*, puts neutrino astrophysics into perspective and relates it to other fields of astronomy. In particular, the various particles are compared with respect to their ability of travelling in straight lines and their tendency to be absorbed by interstellar matter.

Chapter 3 deals with the peculiarities of *Neutrino Astrophysics*. Possible production mechanisms and sources are investigated. Some expected high energy neutrino fluxes that await detection are presented.

In chapter 4 the specific method of high energy *Neutrino Detection* is presented. In particular, section 4.4 explains the AMANDA detector together with some technical details.

The software that is used for *Simulation and Reconstruction* of events in the AMANDA detector is summarized in chapter 5. This is particularly important because the simulation software will be upgraded as part of this thesis as explained in chapter 8. Reconstruction will be important for the understanding of chapter 9.

1.2 Hunting Down Neutrinos

Even with the large efforts that have been undertaken all over the world, the search for extraterrestrial neutrinos with high energies has not yet been successful. The second part of this thesis is therefore mainly about two big leaps that could be made in order to improve the current AMANDA detector. They help to improve our understanding of the detector, and, in particular, of its signal region. This will allow for more sensitive searches in the near future.

Organization of Part II

This part starts with chapter 6, a search for *Angular and Temporal Correlations* in the most recent AMANDA point source sample.

Chapter 7 investigates daily variations found in AMANDA data. The effect is small, but nevertheless, some analysis is done. A non-uniformity of the *Detector Uptime* is found to be the likely cause for the variations.

The understanding of the optical properties of the Antarctic glacier at South Pole has greatly improved over the last few years. In chapter 8 the *Advanced Glacier Modeling* is used for the first time to simulate events in the detector. This allows important investigations of systematic errors of the various analyses.

Chapter 9 introduces a method to specify the relative *Sensitivities of Optical Modules*, which were up to now not known with enough precision. The accurate knowledge is necessary to give a good estimate on the systematic error to analyses.

The *Hollow-Bean-Conjecture* is an unexpected connection relating the analyses in the previous two chapters. Chapter 10 introduces the connection for the explanation of features seen in AMANDA events.

Chapter 11 concludes the thesis by giving an *Outlook* to high energy neutrino astrophysics in general and the work presented here in particular.

Part I

The Context to this Endeavor

Chapter 2

Cosmic Messengers

Intent: Why do we build large and expensive neutrino telescopes in the first place? In this chapter I give a brief overview over the different windows that allow us to observe our Universe. From this it becomes clear why extraterrestrial neutrinos, once detected, are an appealing messenger for astronomy.

Organization: Section 2.1 describes gamma ray astronomy, the high energy extension of optical astronomy. Another window is presented by charged particles, called cosmic rays, which constantly flow onto Earth and also provide a means through which we gain information about our Universe, as described in section 2.2. Other electrically neutral particles such as neutrons present a less useful window, but gravitational waves or dark matter particles one day may become an important messenger (section 2.3). Last but definitely not least, neutrinos pose a very promising new window as described in section 2.4 – and thereafter.

2.1 Gamma Rays

Classical astronomy is of course done with visible light, and for sure the most famous window to our Universe due to its long history and pretty pictures [79, 70]. In a broader sense, classical astronomy is done with light of all wavelengths. Just very recently the *H.E.S.S.* collaboration, which operates atmospheric Cherenkov telescopes in Namibia [44], has made an amazing amount of exciting discoveries (for examples see [8] and [9]) at the high energy end of the electromagnetic spectrum, above 10^{11} eV per photon.

As photons are not deflected by magnetic fields, they have the convenient nature of travelling in straight lines and thus point us the way back to their source. However, photons are easily absorbed: Interstellar dust can absorb light from background sources, and Earth's atmosphere is opaque for photons of most energies. At energies above TeV (10^{12} eV), photons can interact with ambient light and are absorbed when producing electron-positron pairs via photon-photon pair production $\gamma + \gamma_{\text{background}} \rightarrow e^+ + e^-$. Finally, with photons it is not possible to look beyond the Cosmic Microwave Background (CMB).

2.2 Charged Cosmic Rays

In 1912, Victor Hess discovered another kind of extraterrestrial radiation with his ballooning experiments [45]: Charged cosmic rays. This natural source of radioactivity consists mainly of protons, fully ionized helium and electrons. Toward higher energies nuclei of heavier elements contribute more and more to the flux. Today this radiation is measured in great detail by various experiments, as shown in figure 2.1.

The spectrum of cosmic rays extends to macroscopic energies of amazing $10^{20}\,\mathrm{eV} \approx 16\,\mathrm{J}$ per particle. This is many orders of magnitude more than the maximum energy which can currently be examined at particle accelerators: *Fermilab* for example can collide protons and anti-protons, each with an energy of 1 TeV in the center of mass frame. As can be seen by a Lorentz transformation, this corresponds to a cosmic ray proton hitting a stationary atmospheric proton with an energy of only $\approx 2\,\mathrm{PeV}$.

The origin of cosmic rays is still an area of much debate. It is obvious, however, that mechanisms have to exist in the Universe which are capable of accelerating particles to such high energies. Many of these models describe mechanisms which also produce neutrinos of similar energies, and some are introduced in the next chapter. To verify these models it seems natural to directly search for these high energy neutrinos.

When cosmic rays hit Earth's atmosphere, they produce air showers. Protons may react with nucleons of the atmosphere:

$$p + p \rightarrow p + n + \pi^+ \tag{2.1}$$
$$p + n \rightarrow p + p + \pi^- \tag{2.2}$$
$$p + p \rightarrow p + \Lambda + K^+ \tag{2.3}$$

The mesons in turn decay and produce muons as well as neutrinos,

$$\pi^+ \rightarrow \mu^+ + \nu_\mu \tag{2.4}$$
$$\pi^- \rightarrow \mu^- + \bar{\nu}_\mu \tag{2.5}$$
$$K^+ \rightarrow \mu^+ + \nu_\mu \tag{2.6}$$

where the pion decays occur in more than 99% of all cases and the kaon decays in more than 63% [32]. The muons that are produced in these reactions decay with a life time of $2\,\mu\mathrm{s}$ via

$$\mu^+ \rightarrow e^+ + \bar{\nu}_\mu + \nu_e \tag{2.7}$$
$$\mu^- \rightarrow e^- + \nu_\mu + \nu_e \tag{2.8}$$

or they reach the ground where clever physicists may place their detectors to unravel some of the Universe's mysteries. In the search for extraterrestrial neutrino point sources these *atmospheric muons* pose the all-dominating background. However, in their own right they are a signal which can be used for analyses with the Antarctic Muon and Neutrino Detection Array

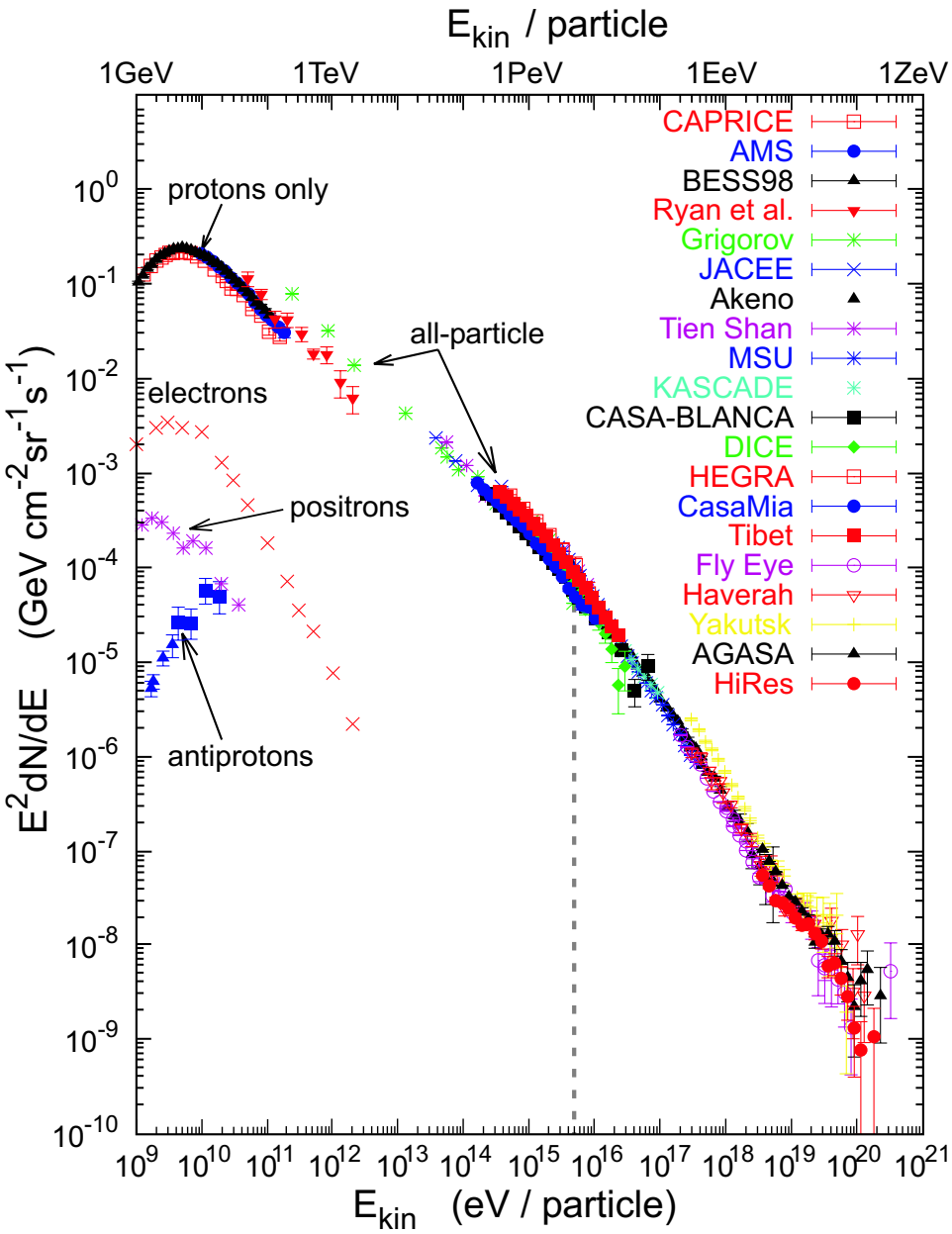

Figure 2.1: The differential particle flux of cosmic rays, multiplied by E^2 so that fluxes that are proportional to E^{-2} appear as a straight line. Diagram generously provided by Tom Gaisser. Note the vast energy and flux range covered by the diagram! On that account, various experiments are necessary to measure this spectrum, as indicated by the different symbols. The spectrum follows a power law $\mathrm{d}N/\mathrm{d}E \propto E^{-2.7}$ for energies between several GeV and PeV. Above about 4 PeV this steepens to a spectrum $\propto E^{-3.1}$ (see e.g. [48, 49]). This kink at about 4 PeV is called the *knee* of the spectrum.

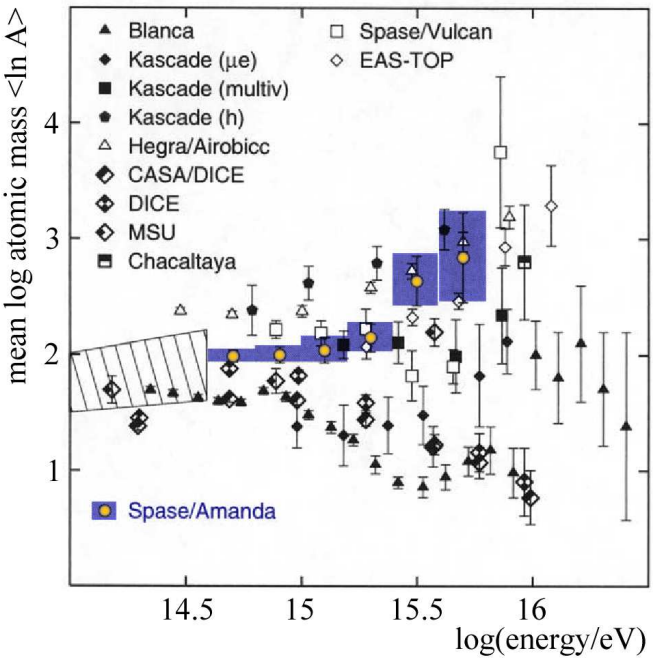

Figure 2.2: The *composition* of cosmic rays around the knee region as measured by various groups. The South Pole Air Shower Experiment SPASE is a scintillator array at the surface near the South Pole. It measures the electron component of the showers that occur when cosmic rays hit the atmosphere. Two kilometers below SPASE, AMANDA measures the muon component of the showers. Operated in coincidence, the primary cosmic ray mass can be estimated. Figure based on [11], SPASE/AMANDA analysis done by K. Rawlins [87].

AMANDA, as shown in figure 2.2. The neutrinos that are produced by cosmic rays in the atmosphere are called *atmospheric neutrinos*.

However, just as photons, charged cosmic rays are not the perfect cosmic messengers either (despite what their name might suggest), mainly out of two reasons:

- Charged cosmic rays are deflected in magnetic fields. Because of the magnetic field of the Milky Way they usually do not point back to their source and may even be trapped within the galaxy. The energy threshold for this to happen is quickly estimated by balancing the centripetal force $mv^2/r \equiv \beta E/r$ with the Lorentz force $qvB \equiv q\beta cB$. A proton with charge $q \approx 10^{-19}$ C in the magnetic field of our galaxy ($B \approx 10^{-10}$ T) is kept in orbit with a radius less than the radius of the galaxy ($r \approx 10^{20}$ m) for energies below $E = qcBr \approx 1\,\mathrm{J} \approx 10^{19}$ eV.

- Above energies of $E \approx 5 \cdot 10^{19}$ eV, cosmic rays interact with photons of the abundant Cosmic Microwave Background (CMB) and produce

the $\Delta(1232)$ resonance which then soon decays into pions:

$$\text{nucleus} + \gamma_{\text{CMB}} \rightarrow \Delta \rightarrow \text{another nucleus} + \pi^{0,\pm} \tag{2.9}$$

Obviously the original energetic cosmic ray is destroyed in this process. The cutoff in the cosmic ray spectrum which is expected due to this mechanism is called the Greisen-Zatsepin-Kuzmin-Cutoff, conveniently abbreviated as GZK cutoff [37].

2.3 Other Cosmic Messengers

2.3.1 Neutral Cosmic Rays

Electrically neutral particles such as neutrons may also serve as cosmic messengers. As they are neutral, they are of course not deflected by magnetic fields.

However, these particles are not stable and therefore only have a limited range. Let's make a rough estimate for this. For example, imagine a neutron (rest mass $m = 1.7{\cdot}10^{-27}\,\text{kg} \approx 1\,\text{GeV}/c^2$) with an energy of $10^{15}\,\text{eV} = 1\,\text{PeV}$, which travels at $(v/c)^2 = 1 - (mc^2/E)^2 \approx 1$. Even during its long life time of $t = 887$ seconds it may only traverse the distance $\gamma v t = E/(mc^2)\, vt \approx 1\,\text{PeV}/1\,\text{GeV}\, c\, 1000\,\text{s} = 3 \cdot 10^{17}\,\text{m} \approx 30$ light years. This is small compared to typical distances at which we expect such high energy particles to be produced: already the center of our Milky Way is almost 30000 light years away.

2.3.2 Gravitational Waves

For the sake of completeness it shall be mentioned that gravitational waves also provide a possible new window to our Universe. Current detectors are approaching the sensitivity to detect some of the known extraterrestrial sources, but hitherto only detect the surf of nearby shores or lumberjacks at work. Although similarities between gravitational wave detectors on the one hand and neutrino detectors on the other may seem plausible for some, I refer to the literature for more on this topic, see e.g. [54].

2.3.3 Dark Matter

In laboratories throughout the world scientists search for Dark Matter. Some use cryogenic detectors which are supposed to absorb the Dark Matter particle and detect it by a faint increase of the detector temperature. These efforts have not yet been successful in detecting any new kind of matter [38, 95]. Complementary to these direct searches, indirect searches also seem promising. Neutrino telescopes like AMANDA can for example be used to search for the annihilation products of dark-matter/dark-matter-reactions as proposed by super-symmetric theories [47].

2.4 Neutrinos

Chapter 3 and the remainder of this work is devoted to very special cosmic messengers: neutrinos. In a sense, neutrinos are the perfect messenger: They are neutral and hence do not interact electromagnetically, so they are not deflected by magnetic fields, travel in straight lines and thus point back to the source. Because of their tiny cross sections, neutrinos are hardly absorbed by interstellar dust or even by whole galaxies. In contrast to photons, neutrinos can provide us with information from remote cosmological areas giving away secrets hidden in the depths of very dense source regions. As they do not decay (although they change their flavor, see section 3.7) neutrinos may traverse the whole Universe. Even the cosmic microwave background does not pose the ultimate horizon for neutrinos and it may one day be possible to observe the era prior to the decoupling of photons and matter.

Neutrinos constitute an entirely different and exciting new window to our Universe. Their detection may reveal wonders undreamed. To this end, it is their very ability to penetrate about everything almost unperturbed, which makes neutrino detection rather difficult. Let us rise to this challenge.

Chapter 3

Neutrino Astrophysics

Intent: Where do high energy neutrinos come from? The most likely process is the acceleration of electrons or protons in astronomical sources by a process called *Fermi acceleration*. These highly energetic particles then interact with ambient particles or photon fields to produce some secondary particles. Mesons are common products if the flux of accelerated particles contains a hadronic component. High energy neutrinos are produced in the decay of these mesons. Propagating the way to our detector, neutrinos undergo oscillations. This chapter will introduce the above mentioned processes.

Organization: The chapter follows the path of neutrinos from the source to the detector. Section 3.1 introduces the Fermi acceleration mechanism. This mechanism is thought to accelerate particles in sources like active galactic nuclei, which are explained in section 3.2. A variety of other possible sources is briefly introduced in section 3.3. Secondary particles with high energies can also be generated in the interaction with the Cosmic Microwave Radiation (section 3.4). Secondary mesons can interact or decay to produce neutrinos, as demonstrated in section 3.5 and 3.6. On the way from the source to our detector, vacuum oscillations of the neutrino flavor occurs, as explained in section 3.7. Section 3.8 introduces the important background contribution of Earth's atmosphere. Finally, some expected fluxes are compared to sensitivities of current experiments in section 3.9.

3.1 Fermi Acceleration

The Fermi acceleration mechanism is the standard way to explain the origin of particles with high energies [41]. The idea is to play ping–pong: The reflection of the ping-pong ball on the moving racket accelerates the ball. Likewise charged particles may be accelerated by moving shock fronts.

The mechanism was originally suggested in 1949 by Enrico Fermi [35]. In an interstellar cloud, magnetic field lines are co-moving with the matter according to the laws of Magnetohydrodynamics. If a slow particle hits such a high-velocity region, the need for thermodynamic equipartition of energy leads to acceleration of this particle as illustrated in figure 3.1. The mean energy gain per bounce is quadratically dependent on the mirror velocity.

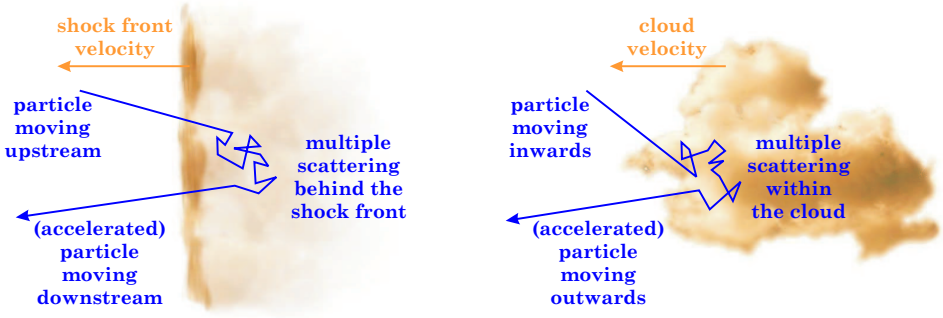

Figure 3.1: Left: In the case of first-order Fermi acceleration, a particle crosses a plane shock front and is accelerated like a ping-pong-ball. The mean energy gain of each crossing depends linearly on the shock's velocity. Right: Originally, Fermi considered acceleration by a moving ionized cloud dragging a magnetic field. This process depends on the cloud's velocity to second order and is therefore called second-order Fermi acceleration.

Thus this process is today called *second-order Fermi acceleration*. In contrast, when the acceleration takes place across a shock front, the energy gain is linearly dependent on the shock velocity. The process is then called *first-order Fermi acceleration*.

When considering the scenarios in more detail, it can be derived (see [35] or the corresponding chapter in [36]) that this scheme leads to an inverse power law for the cosmic ray spectrum and can explain the observed $\mathrm{d}N/\mathrm{d}E \propto E^{-2.7}$ spectrum that was already shown in figure 2.1. The Fermi mechanism even shows a cutoff energy which depends on the rigidity of the accelerated nucleus and can thus cope with the observed knee in the spectrum [11].

Now that we have a mechanism for accelerating particles to high energies, let us see at which locations in the Universe one expects such accelerators.

3.2 Active Galactic Nuclei

The idea of the *Active Galaxy* is an ingenious model which unifies various objects which were previously thought to have nothing in common, like Blazars, Seyfert galaxies, radio galaxies and many other classes [23, 89]. Figure 3.2 is a composite image of an active galaxy at various wavelengths, and figure 3.3 is a schematic drawing of an *Active Galactic Nucleus* according to this unification. The model assumes that an Active Galaxy has a central torus of dust and gas. At the core of the galaxy, a super-massive black hole (with 10^6 to 10^9 solar masses) accretes matter from this torus, which flows inward on an accretion disk. Due to the rotation of the black hole, magnetic field lines get bent at the poles so that highly relativistic jets of

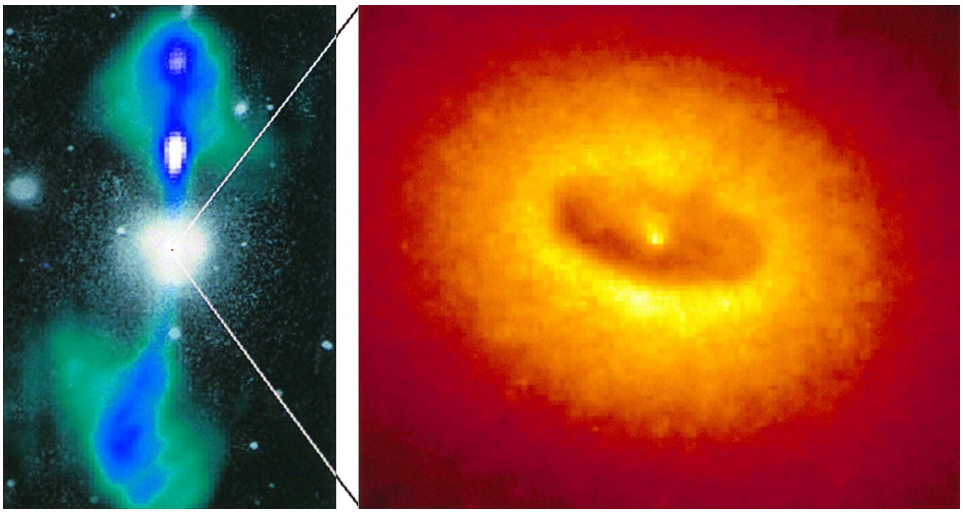

Figure 3.2: NGC 4261, a galaxy with an active galactic nucleus. Left: The galaxy is imaged together with ambient stars and galaxies by a ground-based optical telescope. In green and blue colors, jets as imaged by radio telescopes are superimposed. The width of the image corresponds to roughly 88000 light years. Right: The core of the galaxy, here in orange (false) colors, is imaged by the Hubble Space Telescope. The width of this view corresponds to roughly 1300 light years which is indicated by the dot in the left image. Picture from [81].

matter are ejected along the rotation axis. This process is not yet well understood, but very recent laboratory experiments suggest that it may be quite universal [104].

Active Galaxies are the most luminous objects known and often cover the full electromagnetic spectrum, from radio wavelengths up to ultra-high energy gamma quanta. Typically, the spectrum shows a peak very roughly in the keV-region which is believed to originate from synchrotron radiation, and another peak in the TeV-region. The models that explain the latter peak may be divided into leptonic or hadronic models. In leptonic models, the TeV-γ-peak is due to inverse Compton scattering (section 3.5.1) of relativistic electrons on abundant photons. Hadronic models on the other hand assume the acceleration of hadrons to high energies in jets. These hadrons produce π^0s (among other mesons) which decay into two gamma quanta that may contribute to the observed flux. Whether both leptonic and hadronic processes take place is currently an open question.

Neutrino astronomy holds the key to resolve the quarrel between the two model classes. It allows to distinguish between them as in leptonic models no neutrinos are produced. Only hadronic accelerators yield neutrinos, as will be clear after section 3.5, so a detection of neutrinos from active galaxies would support hadronic acceleration models.

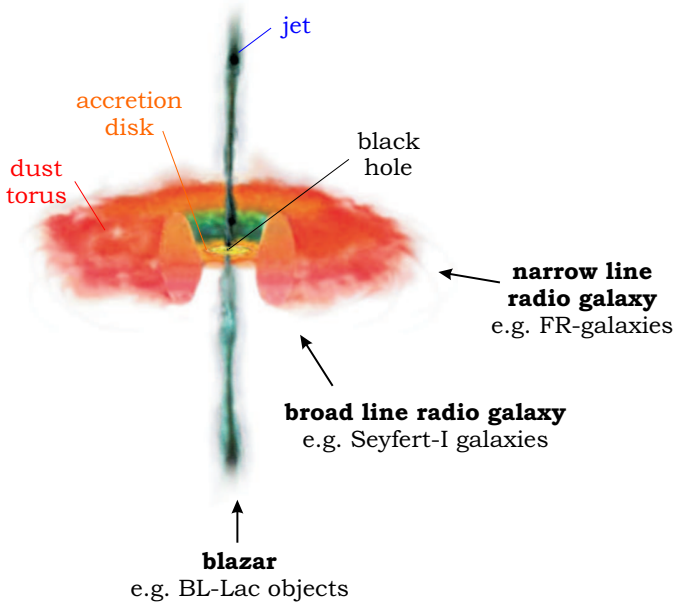

Figure 3.3: A drawing of a typical active galactic nuclei according to the unification scheme. A super-massive black hole sits at the center. It is surrounded by an accretion disk, accreting dust from a torus which surrounds the core. Jets erupt from the center perpendicularly to the accretion disk, aligned with the rotation axis of the object. Dependent on the viewing angle, the object is labeled very differently out of historical reasons, as indicated in the figure. The term *Quasar* applies to very luminous active galaxies that appear point-like in optical telescopes.

3.3 More Possible Sources

3.3.1 Micro-Quasars

A Micro-quasar may be thought of as a baby Active Galactic Nucleus. In this case the mass of the black hole is less than $\approx$ 10 solar masses. The black hole accretes matter from an companion star, such as a red giant. Micro-quasars could also produce significant fluxes of neutrinos.

3.3.2 Supernovae and Supernova Remnants

When a star collapses at the end of its fusion epoch, most of the gravitational energy is emitted as neutrinos in the MeV range. In the case of supernova remnants, observations at radio and hard X-ray wavelengths hint at relativistic electrons being accelerated in shock fronts. If acceleration of hadrons also takes place, relativistic hadrons may react and produce high energy neutrinos.

3.3.3 Pulsars

Pulsars are quickly rotating neutron stars. They may accelerate hadrons to highly relativistic energies, which then may react with the environment to produce high energy neutrinos [18].

3.3.4 Gamma Ray Bursts

These phenomena are not understood very well. In any case, the sources are areas where extremely high energetic processes take place. Naturally, high energy neutrinos may also be produced in such sources.

3.3.5 Weakly Interacting Particles

Weakly Interacting Particles, WIMPs for short, are a popular candidate for Dark Matter, motivated both by particle physics and cosmology. WIMPs may get trapped gravitationally to the core of celestial bodies like the Earth or Sun. There they could annihilate and produce high energy neutrinos.

3.4 GZK Neutrinos

The Greisen-Zatsepin-Kuzmin-Cutoff was already introduced in section 2.2. The corresponding process is the interaction of a proton with a photon from the Cosmic Microwave Background (CMB). Among others, the process

$$p + \gamma_{\mathrm{CMB}} \rightarrow \Delta \rightarrow n + \pi^{+}. \tag{3.1}$$

is possible. Cosmic rays of ultra high energies are indeed observed, they have to propagate and thus this process has to take place. As its products are unstable and decay, this leads to a virtually guaranteed neutrino flux with an uncertainty of only one order of magnitude, plotted later in section 3.9. The Greisen-Zatsepin-Kuzmin neutrino flux is too low for the current AMANDA sensitivity, but the cubic-kilometer sized IceCube detector which is being constructed at South Pole will be able to detect it.

3.5 Interactions of Primary Particles

Electrically charged particles like electrons, protons or heavier nuclei are the primaries that are accelerated to high energies. They can interact in a variety of reaction channels and produce high energy photons or mesons.

3.5.1 Inverse Compton Effect

Here, a high energy electron scatters on a low energy photon. This low energy photon can be from the ambient photon field, it may be a synchrotron photon, or it can be from the abundant Cosmic Microwave Background. In

the inverse Compton process, the electron boosts a gamma quantum to higher energy:

$$e^- + \gamma_{\text{low energy}} \longrightarrow e^- + \gamma_{\text{high energy}}. \tag{3.2}$$

This high energy quantum can be observed with the appropriate telescopes. No neutrinos are produced in this channel, a general feature of leptonic acceleration models.

3.5.2 Photon-Meson-Interaction

Protons may be excited into delta-resonances in processes like

$$p + \gamma \longrightarrow \Delta^+ \longrightarrow p + \pi^0 \tag{3.3}$$
$$p + \gamma \longrightarrow \Delta^+ \longrightarrow n + \pi^+ \tag{3.4}$$

where the resonances quickly decay and produce pions.

3.5.3 Proton-Proton-Interaction

Protons may interact directly to produce pions:

$$p + p \longrightarrow \pi^0/\pi^+/\pi^- \tag{3.5}$$

So after the initial acceleration we are left with highly relativistic, stable particles like protons that leave the source and constitute the cosmic ray flux, and furthermore, with highly energetic unstable particles like mesons that will soon decay.

3.6 Decay of Secondary Particles

The decay of a π^0 results in high energy gamma quanta:

$$\pi^0 \longrightarrow \gamma + \gamma \tag{3.6}$$

which are detectable by gamma ray telescopes. The decays of charged pions are of more interest here as they result in high energy neutrinos:

$$\begin{aligned} \pi^+ &\longrightarrow \mu^+ + \nu_\mu \\ &\quad\ \mu^+ \longrightarrow e^+ + \nu_e + \bar{\nu}_\mu \end{aligned} \tag{3.7}$$
$$\begin{aligned} \pi^- &\longrightarrow \mu^- + \bar{\nu}_\mu \\ &\quad\ \mu^- \longrightarrow e^- + \bar{\nu}_e + \nu_\mu \end{aligned} \tag{3.8}$$

From pion decay we thus expect the neutrino flux to be produced in a flavor ratio

$$F(\nu_e) : F(\nu_\mu) : F(\nu_\tau) = 1 : 2 : 0 \tag{3.9}$$

where no distinction is made for antiparticles or the different energies. It is those neutrinos that give the expected signal for neutrino telescopes like AMANDA. They require hadrons to be accelerated and thus rule out, once detected, purely leptonic acceleration models where no neutrinos are produced.

3.7 Propagation of Neutrinos: Oscillations

It is now widely accepted that neutrinos indeed have a small mass. The current limit for the sum of the mass of the three neutrino flavors is $0.05\,\mathrm{eV} < \Sigma m_{\nu_l} < 0.42\,\mathrm{eV}$ [97]. Just like quarks, neutrinos undergo oscillations [64, 68, 88] because their flavor eigenstates $|\nu_l\rangle$ are not identical to the mass eigenstates $|\nu_i\rangle$ but a superposition of these:

$$|\nu_l\rangle = \sum_i U_{li} \, |\nu_i\rangle \tag{3.10}$$

where U_{li} is the Maki-Nakagawa-Sakata (MNS) matrix, the analogue to the Cabibbo-Kobayashi-Maskawa (CKM) matrix known from the quark sector. Mixing occurs because the mass eigenstates have different energies and thus different time development $\mathrm{e}^{-iE_i t/\hbar}$.

This means that the 1:2:0 ratio (equation 3.9) at the source is not what we should expect here on Earth. Instead, over long distances, the oscillation length is small compared to the traveled distance and the ratio smears out. We are then left with

$$F(\nu_e) : F(\nu_\mu) : F(\nu_\tau) = 1 : 1 : 1 \tag{3.11}$$

independent of energy [17]. This is important when comparing theoretical predictions to experiments: Experimental flux limits always quote the fluxes on Earth. For the muon-neutrino based point source searches with AMANDA this means that the models are restricted less stringently by a factor of two.

3.8 Contributions from the Atmosphere

Charged cosmic rays hitting the atmosphere can produce pions or kaons. These mesons may either hit air nuclei or they may decay to produce atmospheric muons and neutrinos (e.g. $\pi^+ \longrightarrow \mu^+ + \nu_\mu$).

The spectrum of the atmospheric muons follows that of the primary cosmic rays. Therefore they have a steeply falling (*soft*) spectrum $\mathrm{d}N/\,\mathrm{d}E \propto E^{-2.7}$ below $E \approx 100\,\mathrm{GeV}$ which steepens even more above these energies, where $\mathrm{d}N/\,\mathrm{d}E \propto E^{-3.7}$. The reason for the softening of the spectrum is that the decay length of pions $d = \gamma c\tau = E/(mc^2)\, c\tau$ increases linearly with energy, whereas the interaction length is only weakly energy dependent. Thus with higher energies, more and more pions interact instead of decaying and so do not produce muons.

The same line of argument applies to the atmospheric neutrinos that are produced in atmospheric meson decays. Thus atmospheric neutrinos have a soft spectrum that goes like $\mathrm{d}N/\,\mathrm{d}E \propto E^{-3.7}$ above $\approx 100\,\mathrm{GeV}$.

Now that we have an idea about possible sources and production mechanisms, let us have a look at the expected neutrino fluxes.

3.9 Flux Predictions

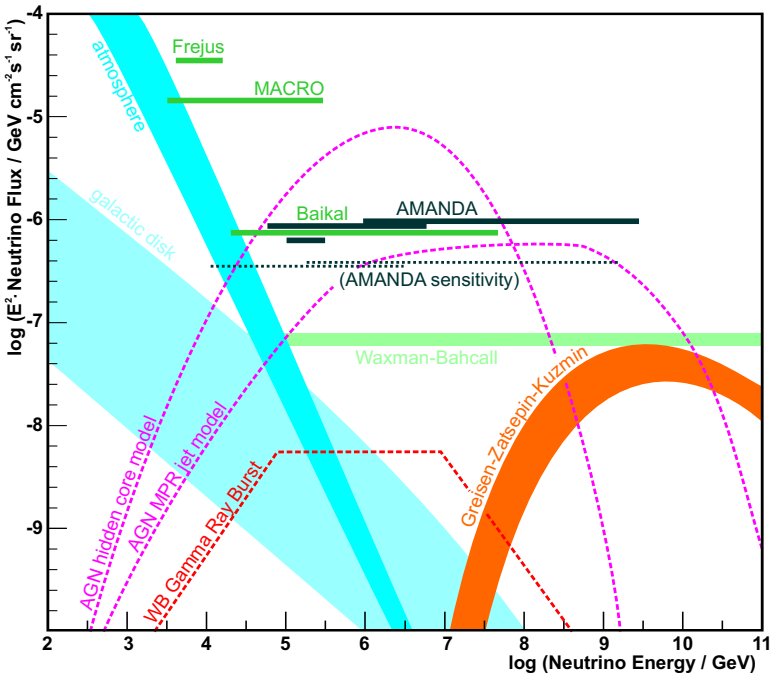

Figure 3.4: Various neutrino fluxes and limits. The diagram follows the standard way of multiplying the fluxes by E^2 so that a spectrum $\propto E^{-2}$ shows up as a flat line. In blue, the atmospheric and expected galactic neutrino fluxes are plotted. The guaranteed but yet undetected Greisen-Zatsepin-Kuzmin neutrino flux is shown in orange, the Waxman-Bahcall upper bound for extragalactic sources is shown in light green. In red dashed lines, three examples for model predictions are shown. The measured limits of AMANDA are shown in dark green, those of some other neutrino detectors in light green. The sensitivities of ongoing AMANDA data analysis is shown as dotted lines. For similar plots see [66, 91].

Pion decays lead to both gamma quanta (from π^0) and neutrinos (from $\pi^{\pm}$). The flux of gamma quanta is measured, so that one can estimate expected neutrino fluxes by normalizing models to this gamma ray flux [66]. Figure 3.4 shows some expected (or measured in the case of atmospheric neutrinos) fluxes together with limits as determined by various detectors.

From the cosmic rays flux, Waxman and Bahcall derived an upper limit on the muon neutrino flux that can be expected from extragalactic sources [100]. The idea is that primary particles like protons are accelerated in thin sources in which they can interact only once before they escape. As the proton flux on Earth is measured, and the possible interaction processes are known, this allows to estimate a flux of muon neutrinos, at least for some standard models that come without special assumptions. The

limit set by Waxman and Bahcall is around $4 \cdot 10^{-8}\,\mathrm{GeV\,cm^{-2}\,s^{-1}\,sr^{-1}}$ for muon neutrinos without oscillation. With oscillations this becomes a factor of two smaller, and in the all-flavor plot 3.4 a factor of three larger, thus $6 \cdot 10^{-8}\,\mathrm{GeV\,cm^{-2}\,s^{-1}\,sr^{-1}}$.

Chapter 4

Neutrino Detection

Intent: As we have seen, neutrinos are indeed interesting cosmic messengers. They may provide us with information that we could not gain otherwise, such as the distinction between different acceleration mechanisms. Once we have decided that we want to detect high energy neutrinos, let us consider how to build a detector for them.

Organization: Section 4.1 is about the rare interaction of neutrinos, which lead to the corresponding charged leptons. These leptons then give a light signal that can be detected as described in section 4.2. Some historical remarks on high energy neutrino detectors are written up in section 4.3, and the AMANDA detector is introduced in the following section 4.4. In particular, section 4.4.4 is about the relevant optical ice properties of the South Pole glacier.

4.1 Neutrino Reactions

Neutrinos can not interact electromagnetically, but through the weak interaction by the exchange of $W^{\pm}$- or Z^0-bosons. The major interactions are charged and neutral current reactions of the kind

$$\nu_l + N \longrightarrow l + X \quad \text{(CC)} \tag{4.1}$$

$$\nu_l + N \longrightarrow \nu_l + X \quad \text{(NC)} \tag{4.2}$$

where l represents any lepton e, μ or τ and the nucleon N is transferred into another hadronic state X. The cross sections for these reactions are very small (see figure 4.1, so a very large target is needed to detect cosmic neutrino fluxes. From the HERA data in figure 4.1 the neutrino cross sections are thought to be known and well behaved up to $5 \cdot 10^3$ GeV. However, here we have to deal with energies up to 10^{11} GeV. The cross sections at these energies are educated extrapolations within the framework of electroweak theory. Figure 4.1 also shows these extrapolations as they are used in the AMANDA simulations.

For neutrino telescopes one distinguishes between the muon channel (based on $\nu_\mu + N \longrightarrow \mu + X$), and the cascade channel (based on all other reactions 4.1 and 4.2). In the latter case, the hadrons, electrons or taus

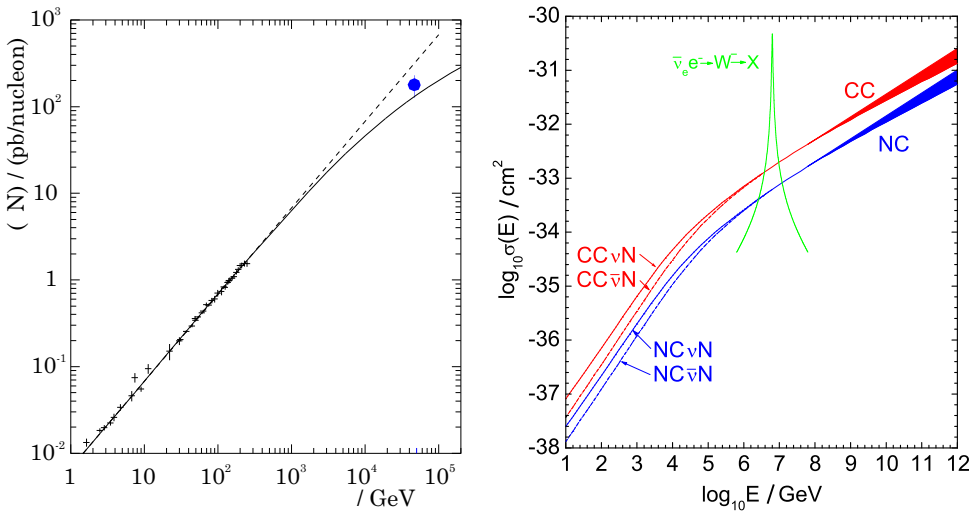

Figure 4.1: Left: Direct measurements of the total neutrino-nucleon cross section together with a value at about $5 \cdot 10^4$ GeV calculated from the HERA experiments [57]. Right: Educated extrapolations of the neutrino cross sections to energies relevant for high energy neutrino telescopes. The so-called Glashow resonance (shown in green) in the $\bar{\nu}_e$-channel at energies around 10^7 GeV is due to resonant W-boson production [34]. At even higher energies, models at hand differ up to a factor of two. Figure adopted from [39].

produce particle showers and deposit their energy within a few meters only. For the standard high energy neutrino detectors this results in a good energy resolution but bad directional information about the original neutrino.

To do neutrino astrophysics, one would like to be able to infer the direction of the neutrino. Muons produced in the muon channel may travel distances of the order of kilometers, therefore providing a very good handle on the directional information. But an angular resolution of about 1° is only possible for neutrino energies above a few 100 GeV (see figure 4.2). Although this poses an ultimate limit for the precision of neutrino telescopes, this requirement is not as bad as it might look at first: The expected flux of such high energy neutrinos is still large enough to be detectable soon. The neutrino cross section increases with energy. Plus, the secondary muon's track length increases with energy making a reliable detection easier. In what follows I will focus on the muon channel, and the presented analyses are all done using muons. For more on the cascade channel the reader is referred to the thesis of Marek Kowalski [58].

4.2 Muon Propagation

4.2.1 Energy Losses

Muons travelling through ice suffer from a variety of energy losses. Energy is continuously lost through ionization of the ice according to the Bethe-

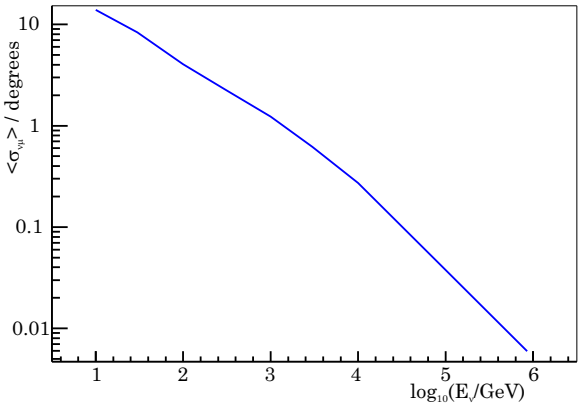

Figure 4.2: The mean scattering angle between neutrino and muon, taking into account all neutrino-nucleon interactions. Data from [42].

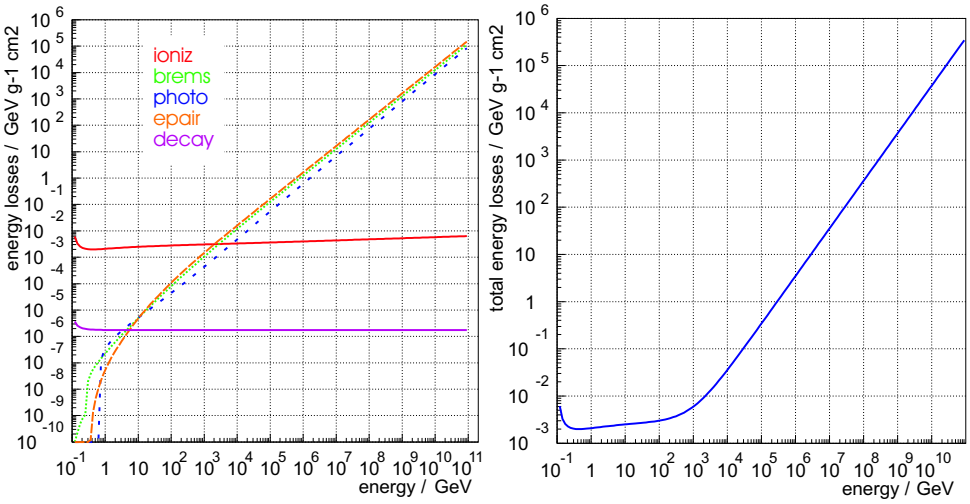

Figure 4.3: Energy losses for muons of different energies propagating through ice. Left: The contributions of the different mechanisms: Ionization, bremsstrahlung, photo-nuclear processes, pair production or the decay of the muon. Right: Sum over these contributions. Figures taken from [28].

Bloch formula (see e.g. [32], chapter 27). At the high energies relevant here, stochastic processes become equally important, like bremsstrahlung, e^+e^-–pair production, and photo-nuclear interactions where muons interact with nuclei by the exchange of a virtual photon. Muons may be inelastically scattered and eventually they may also decay within the detection volume. The differential energy losses as implemented in the AMANDA simulation are shown in figure 4.3.

4.2.2 Cherenkov Light

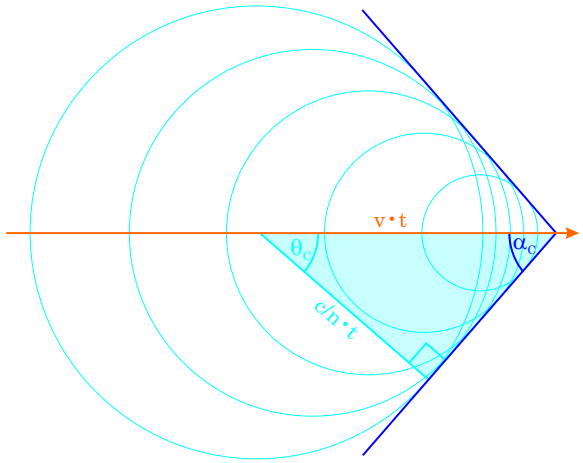

Figure 4.4: The Huygens construction to formula 4.3.

When a charged particle travels through a transparent medium with refractive index n, it emits Cherenkov light if the particle's velocity v exceeds the speed of light in the medium c/n. Cherenkov photons are emitted under an angle θ_c satisfying

$$\cos\theta_c = \frac{c/n}{v} = \frac{1}{\beta n} \tag{4.3}$$

which can be easily seen from the Huygens construction in figure 4.4. The Cherenkov photons form a cone as sketched in figure 4.5 with an opening angle α_c satisfying [76]

$$\cot\alpha_c = \sqrt{\beta^2 n_0^2 - 1} + \frac{n_0\omega_0\beta^2}{\sqrt{\beta^2 n_0^2 - 1}} \frac{\mathrm{d}n}{\mathrm{d}\omega}\Big|_{\omega_0} \tag{4.4}$$

in the case that the light follows a narrow distribution centered around a frequency ω_0 (see [96] for the original derivation). In a non-dispersive medium, the second term in equation 4.4 is zero and the opening angle α_c is the complement of θ_c.

The refractive index of ice is $n \approx 1.32$, giving a Cherenkov angle of $\theta_c \approx 41°$. A significant contribution to the light output comes from secondary

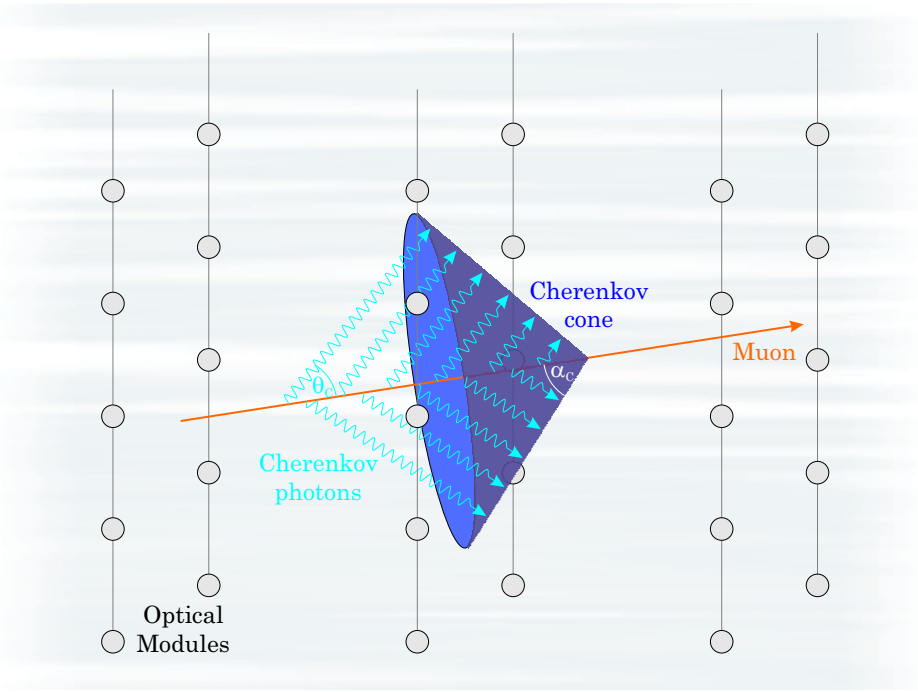

Figure 4.5: A charged particle travelling through a medium faster than the local speed of light c/n emits Cherenkov photons which form the so-called Cherenkov cone. Here, a muon travels through a non-dispersive medium, so that the with opening angle α_c equals $90° - \theta_c$. In high energy neutrino detectors, this blueish Cherenkov light is detected with a grid of photomultipliers.

particles like knock-on- (δ-) electrons, which are also highly relativistic. For muons ($m \approx 106\,\mathrm{MeV/c^2}$), the threshold to produce Cherenkov radiation is quickly estimated to be $E^2 > m^2c^4(1 + 1/n^2)$, that is, $E \gtrsim 135\,\mathrm{MeV}$.

4.3 History and Other Experiments

Many different designs that were studied for neutrino detectors were found not to work (see e.g. [65]). Radio and acoustic detection of neutrinos will be possible soon [16]. First ideas for neutrino detectors using Cherenkov radiation came from Andrei Markov in the Soviet Union in 1959 [71], and from Kenneth Greisen in the United States who published his proposal in 1960 [40].

In the 1970s it became clear that the small fluxes together with the tiny neutrino cross sections make it necessary to "turn the Earth itself into a great neutrino detector" [105] and use what nature provides as target material. For optical detectors, transparent media like glaciers, oceans or lakes can serve as detection volume. The task is to detect the Cherenkov light emitted

by secondary particles as they traverse this volume (figure 4.5). This is done by a matrix of so-called *optical modules*, each containing a photomultiplier and some electronics.

DUMAND was the first project to start in the 1970s off shore Hawaii, but it never made it much beyond the deployment of a first string of optical modules. Since the 1990s, the Baikal neutrino telescope has been operated in Lake Baikal, Siberia. It was successfully upgraded and extended this year. The advantage at Lake Baikal is that it freezes over winter, so that heavy deployment machines can be used.

In the Mediterranean sea, ANTARES started to take data with first test strings. The NESTOR and NEMO projects are running in the R&D phase, and a Mediterranean cubic-kilometer sized detector (KM3NeT) is under investigation. The major difficulty for all these projects is the deployment of the strings under maritime conditions, so no competitive results from open water telescopes are expected before 2007.

At the South Pole, the AMANDA detector is taking data. A first string of the cubic-kilometer-sized successor IceCube operates very successfully.

4.4 AMANDA

4.4.1 General Remarks

The Antarctic Muon and Neutrino Detector Array (AMANDA) [14, 15, 19] uses the glacier at the South Pole as a detection volume and the Amundsen-Scott South Pole station for infrastructure purposes. Once personnel and equipment is flown to the pole, heavy machinery can be used for deployment. The holes for the strings that support the optical modules are melted into the glacier using hot water. Once the hole is completed, the drill head is pulled up and the string with the optical modules is lowered in the water-filled hole. Within a few days the hole refreezes and the modules are fixed in position. It is clear that they can not be recovered once deployed.

The first four AMANDA strings were deployed in the Antarctic summer 1993/1994 after some site studies in the previous years. The depth of these strings (AMANDA-A) reached only one kilometer. As it turned out, the ice at these depths is not suitable for our purposes: Air bubbles trapped within the glacier lead to scattering lengths of only $\approx 25\,\mathrm{cm}$, and AMANDA-A could only be used for limited purposes.

Luckily, with increasing pressure, these air bubbles are compressed and integrated in the lattice structure of the ice. This structure is called a solid *air-hydrate clathrate phase* [74, 84]. As it happens, these clathrates have almost identical refraction indices as ice ($n_{\mathrm{clathrate}}/n_{\mathrm{ice}} \approx 1.004$) and thus do not worsen the scattering or absorption lengths [103]. Hence in 1995/1996, four new strings were deployed to depths up to 1950 m. Over the next few years, more and more strings were installed: Strings 5–10 in 1996/97, strings 11–13 in 1998/99 and strings 14–19 in 1999/2000. Thus the detector reached its present state, labeled AMANDA-II: 677 optical modules on 19

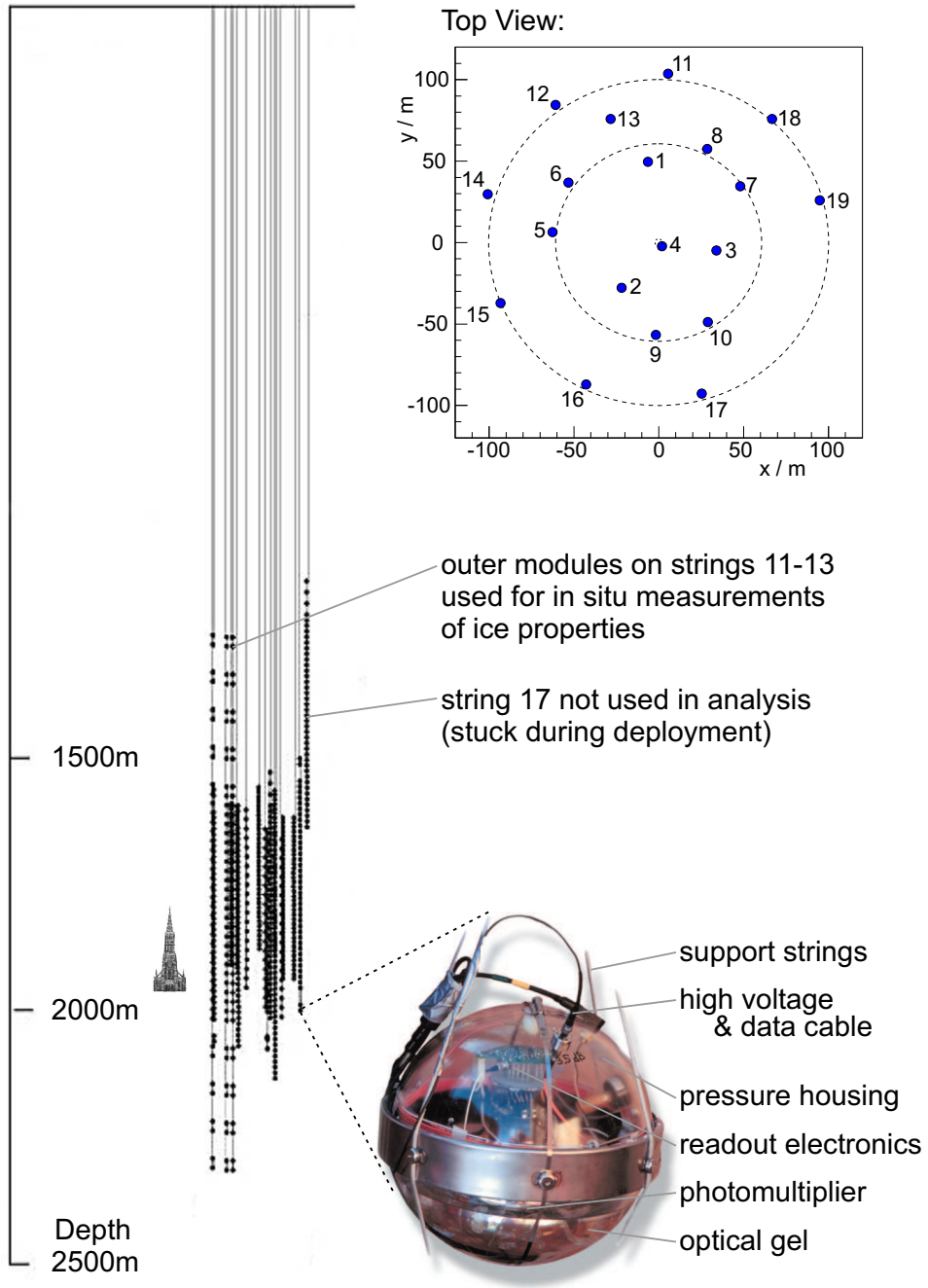

Figure 4.6: A sketch of the AMANDA-II detector, drawn to scale together with the world's highest steeple, the Münster of Ulm. In the upper right a top view with the locations of the 19 strings that compose the detector. In the bottom right one of the 677 optical modules with its most important constituents labelled. The upper half of the optical module is dominated by high voltage support and readout electronics, on the lower half the photomultiplier entry glass and the contact gel can be seen.

strings make up this telescope. As the detector has grown over many years and is also intended to test different devices, it has quite an inhomogeneous topology, as sketched in figure 4.6.

AMANDA strings are separated from each other by $30-60\,\mathrm{m}$ (see upper right of figure 4.6), whereas along a string the optical modules are separated by 10–20 m. This sparse arrangement is necessary simply to reduce the cost of the detector, and sufficient to reconstruct a muon's direction. However, the energy information is hardly inferable, which is easily seen when one compares the light collecting area of the photomultipliers to the shell of the whole detector array,

$$\frac{N\,A}{2\pi\,r\,h} \approx \frac{600 \cdot 0.0284\,\mathrm{m}^2}{2\pi \cdot 200\,\mathrm{m} \cdot 500\,\mathrm{m}} \approx 3 \cdot 10^{-5}, \tag{4.5}$$

so only a tiny fraction of the total light output is recorded. In ice, the propagation of light is scattering limited, so it is very important to know the detection medium as precisely as possible [75].

With its specific location, the experiment attracts a big public interest (recently e.g. in Berlin with exhibitions on the occasion of the Lange Nacht der Wissenschaften and the Einstein exhibition) and allows to introduce a broad audience to this rather exotic physics topic (e.g. [90]). The successful operation of the detector made the path free for the construction of a second generation neutrino telescope called IceCube. The first string of this telescope was deployed this year. Once finished (around 2010), IceCube will span a volume of one cubic kilometer with almost 5000 optical modules, each containing a small computer on its own.

4.4.2 Signal Readout

The optical modules in AMANDA are purely analog devices. To send the photomultiplier signal to the surface a variety of cables is used: coaxial cables are used for the inner four strings and twisted pair cables for strings 5–10. Strings 11–19 are equipped with optical fibers and with twisted pair cables as backup.

Once at the surface, the signals digitalized: An Analog-to-Digital-Converter (peak-ADC) records the peak value of the pulse while a Time-to-Digital-Converter (TDC) records a start and end time for each pulse [67]. The full event is written to disk if a trigger condition is fulfilled. Most importantly, the event is written if 24 optical modules have a hit within a time window of $2.5\,\mu\mathrm{s}$ (a value which may be compared to $500\,\mathrm{m}/(3 \cdot 10^8\,\mathrm{m/s}) \approx 1.7\,\mu\mathrm{s}$). The trigger rate in AMANDA as of 2004 is around 80 Hz but varies within different years (because of different detector setups) and seasons (because of different atmospheric densities, as discussed in the next section).

4.4.3 Signal and Background

Figure 4.7 shows a schematic view of the position of the AMANDA detector, together with the major signal and background contributions. AMANDA

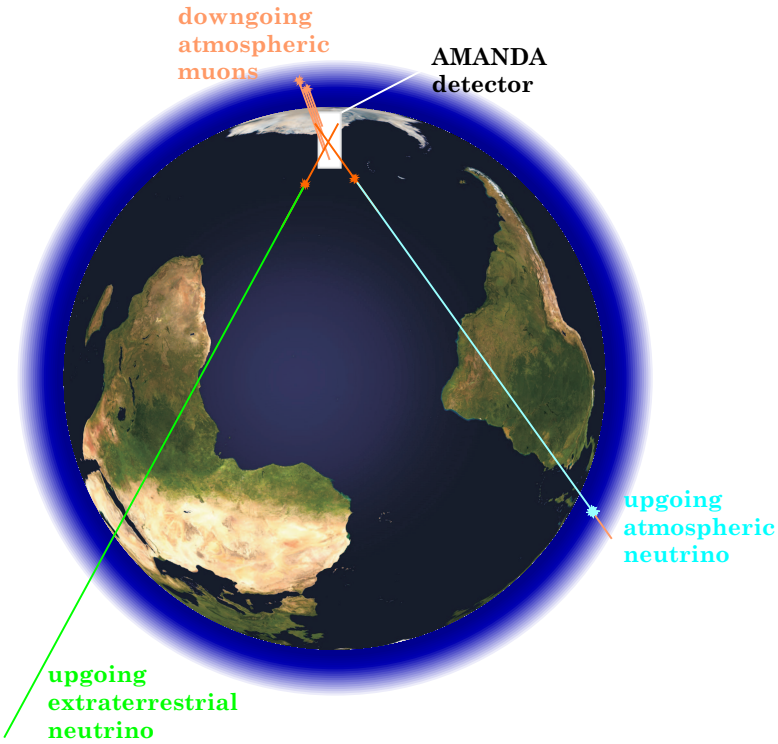

Figure 4.7: To the definition of *up-going* and *down-going* events: Atmospheric muons (light orange) are the major background for any neutrino detector. In AMANDA they are also referred to as down-going events. Muons are not able to penetrate Earth, so our planet can be used as a filter: Upward moving muons have to originate from neutrinos, as they can cross the Earth and may interact close to the detector to produce the detected up-going muons. These neutrinos are either produced in the atmosphere or may even be of extraterrestrial origin.

records about 10^9 events each year which are mostly down-going muons. Out of these, about 10^3 up-going neutrino candidates can be extracted. With this signal to noise ratio of $1 : 10^6$ the major challenge of the project is evident. In particular, each year about 10^6 down-going atmospheric muons are misreconstructed as up-going muons. Figure 4.8 is an illustrative example.

The mean range of muons is plotted in figure 4.9. A 1000 GeV muon in ice travels about 2 km before it is stopped. Therefore, atmospheric muons can penetrate the South Polar ice quite easily and trigger the AMANDA detector with ≈ 80 Hz. With this high trigger rate, atmospheric *down-going* muons constitute the major background. The muon distributions show a strong dependence on the zenith angle and are highly suppressed at zenith angles $\theta \gtrsim 80°$ (close to the horizon) because of the longer distance traveled through the glacier. The trigger rate shows a seasonal variation of about $\pm 10\%$ [22] because higher temperatures in summer mean a lower density in

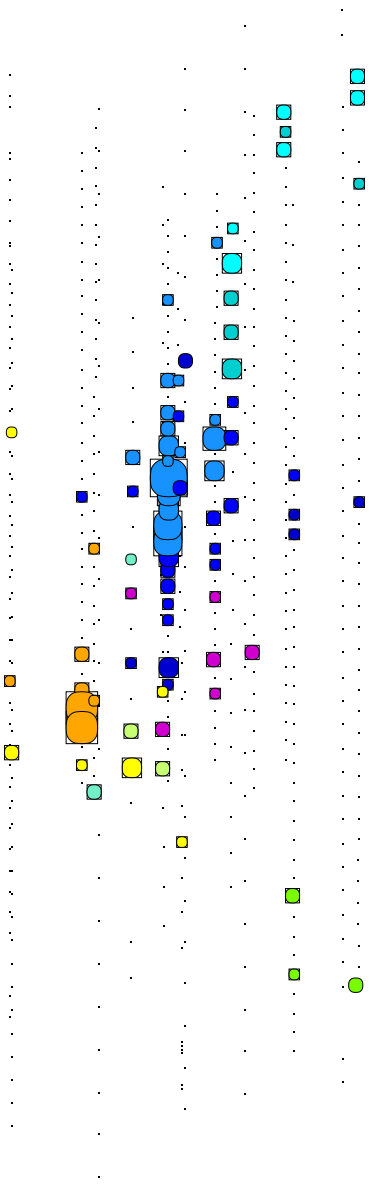

Figure 4.8: A true event recorded by AMANDA on April 22, 2000, showcased by collaborator Sebastian Böser in his thesis [22]. The black dots indicate the optical modules of AMANDA. The colors indicate the time of a hit, from orange (early) to violet (late), and the sizes of the circles scale with the corresponding ADC peak values. What was recorded here? At first one might say that this is a noisy record of an up-going neutrino's muon coming from the lower left and traversing the detector to the upper right. However, one might also recognize that two down-going muons are recorded here as one event, the first going from middle left to lower right, the second from upper right to the middle. It is the challenge for the experiment's software to find out the correct possibility.

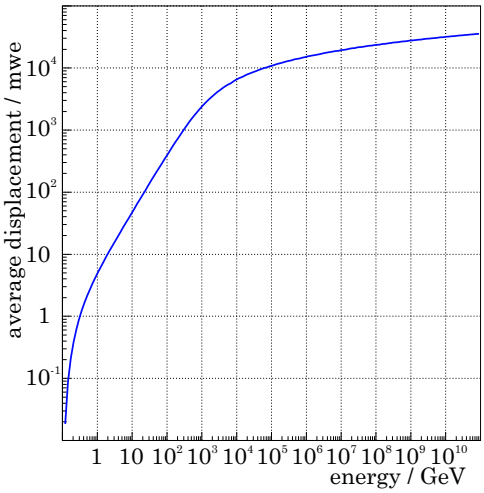

Figure 4.9: The average distance that muons can travel in water, in units meter water equivalent (mwe), from [28].

the atmosphere and therefore an increased probability for pions to decay, thus leading to more muons.

Decays of cosmic ray induced mesons lead to so-called *atmospheric neutrinos*. In the detector, these neutrinos show no zenith angle dependence as they can penetrate matter almost unperturbed. They serve as major calibration source to the detector. Recently atmospheric neutrinos have been analyzed regarding possible seasonal variations [1]. For extraterrestrial searches [3] however they constitute a major background. So doing astronomy with AMANDA is like raising one's face to observe the stars during daytime: Although this sounds impossible at first, with a telescope that is sensitive enough this is conceivable.

4.4.4 The Detection Medium

AMANDA uses Antarctic ice as a detection medium. This has some advantages and disadvantages when compared to water as detection medium, as used in the Baikal experiment or by the Mediterranean attempts. A short comparison shall be given:

- A major advantage turns out to be the comparatively easy deployment of the optical modules. Heavy equipment may be used at the South Pole. The readout electronics can be set up very conveniently on the surface; in contrast to water experiments it is not necessary to bridge a long distance to the shore. The design of electric feed-throughs at the optical modules is rather easy, as they are surrounded by solid ice after only a few days. Water based detectors have to use delicate electric plugs and even may need robot submarines for deployment.

- Typical Cherenkov light absorption is much smaller in ice detectors

than in water detectors. In AMANDA, typical absorption lengths are of the order of $\lambda_a \approx 100\,\mathrm{m}$, where the ANTARES collaboration reports $\lambda_a \approx 20\,\mathrm{m}$ [7].

- Typical noise rates of the optical modules are much lower in ice: In AMANDA, typical noise rates are around 1 kHz, whereas in ANTARES the noise rates are above 100 kHz due to ^{40}K decays in ocean water — and they even can go up another factor of 10 due to bio-luminescence [7].

- A disadvantage of ice as detection medium is the rather small scattering length compared to water telescopes. While the South Pole glacier has effective scattering lengths (see below for a definition) of the order of $\lambda_{\mathrm{eff}} \approx 20\,\mathrm{m}$, the Mediterranean sea has $\lambda_{\mathrm{eff}} \approx 120\,\mathrm{m}$. I turn this to our advantage in the analysis presented in chapter 9.

- The optical properties of Antarctic glacier ice vary with depth. This causes some interesting effects and has to be considered in the modeling of the detector. The remainder of this section and chapter 8 address this issue.

The varying optical properties of the detection medium are parametrized by the absorptivity and the effective scattering coefficient. The absorptivity, sometimes also called absorption coefficient, is the reciprocal of the absorption length λ_a, where the absorption length is simply defined as the distance at which the survival probability of a photon drops to $1/e$.

In AMANDA, one always has to deal with multiple scatterings, as the distance between optical modules is large compared to the scattering length λ_s. Therefore λ_s or the average scattering angle $\langle\cos\theta\rangle$ are not measurable individually. However, one can measure the effective scattering length λ_{eff}, which combines λ_s and $\langle\cos\theta\rangle$ to

$$\lambda_{\mathrm{eff}} = \frac{\lambda_s}{1 - \langle\cos\theta\rangle} \tag{4.6}$$

as derived e.g. in [103]. The effective scattering length can be pictured as follows: Imagine a cloud of photons travelling in a medium that scatters isotropically. Then the scattering length λ_s is the distance at which, due to scattering, the photon cloud has lost its average velocity. Now, scattering in ice is not isotropically but strongly forward peaked. So after a scattering length λ_s, the photon cloud would still have a substantial amount of its initial average velocity. The effective scattering length λ_{eff} is defined as the distance after which the photon cloud has indeed lost its average velocity. Only for isotropically scattering media is $\lambda_{\mathrm{eff}} = \lambda_s$. The effective scattering coefficient is simply the reciprocal of λ_{eff}.

To investigate the optical properties of the detection medium in detail, light sources are installed with the AMANDA detector. Pulsed light sources are a frequency-doubled Nd:YAG laser on the surface with optical fibers

leading down every string, two nitrogen lasers deployed in pressure spheres, and eight beacons with six blue LEDs each deployed on the longer strings. Also, there is a 20 W Xenon arc lamp at a depth of about 1850 m and a *Rainbow Module* where the light of a Halogen lamp is beamed through a grating. Each of the new IceCube digital optical modules has 12 LEDs with it for calibration purposes.

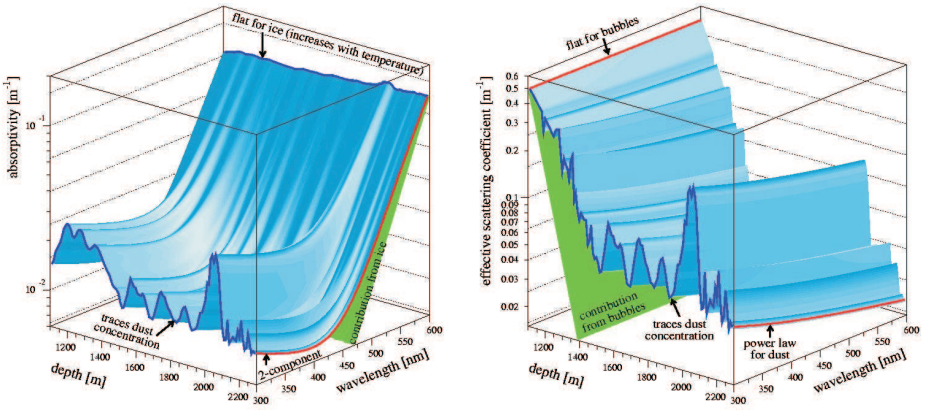

Figure 4.10: Left: The absorptivity of AMANDA ice versus depth and wavelength traces climatological changes over the last 60,000 years. In green the contribution of pure ice which becomes dominant for long wavelengths. Right: The effective scattering coefficient of AMANDA ice versus depth and wavelength also tracks climatological changes. At shallow depths, the contribution of air bubbles becomes dominant. Figures from [102].

With these devices, it is possible to measure the optical properties of the ice with great precision [98, 103]. The understanding of the full depth and wavelength dependent behavior of these parameters is now quite advanced. Figure 4.10 shows the absorptivity and the effective scattering coefficient of AMANDA ice in the relevant ranges. Both parameters show an articulate variation with depth.

The reason is the slow growth of the glacier. At South Pole, a small annual snowfall causes the glacier to accumulate. The snow is compressed under its own weight and undergoes a transition to ice. Only small amounts of impurities can reach the Pole by wind. As it turns out, Antarctic ice at these depths is the most transparent natural medium known and has only little contaminations. The few impurities cause a depth dependent, layered structure that needs to be accounted for in a proper modeling of the ice parameters. Main contributions come from soot to absorption, from sea salt crystals to scattering and insoluble mineral grains to both scattering and absorption.

The Glaciological community showed strong interest in measurements of ice properties done by our collaboration [85]. Investigations of Antarctic ice drill results allow climatological models and temporal investigations over

the last 500.000 years [33, 83] which can be related to our results. Thus it is concluded that AMANDA is embedded in ice that is 30.000 to 60.000 years old. Individual layers of ash from historic volcanic activity were long conjectured but identified just very recently with a dedicated method [24].

Chapter 5

Simulation and Reconstruction

Intent: As seen in the previous chapter, it is important to know which signal in the detector one has to expect from different particles. This is inferred from *simulation* software. *Reconstruction* software is used to deduce the most likely particle properties from a signal. This chapter introduces the corresponding programs that are commonly used in the AMANDA experiment.

Organization: Section 5.1 introduces the various programs that are used to simulate the detector, from cosmic rays hitting the atmosphere to the electrical readout system. Section 5.2 explains some of the reconstruction algorithms that are implemented in the software.

5.1 Simulation Software

As is customary, the term *Monte Carlo* (MC) is used interchangeably with computer *simulations*, since the casino in Monaco exhibit random events just as the software does. The simulation of the AMANDA detector is done in a chain of subsequent steps, each performed by individual software packages. The chain itself is supervised by a series of `Perl` scripts called `Simuperl` [31], and the events are passed in the AMANDA specific *format 2000* (`.f2k`) plain-text format [94].

5.1.1 Muon Generator

To simulate atmospheric muons from highly energetic cosmic ray particles, the standard software package is `Corsika`, the *COsmic Ray SImulations for the KAscade experiment* [43]. For AMANDA, this software is modified to comply with the specific requirements and the internal data format, and is then called `dCorsika` [26, 29]. The software simulates the flux of cosmic rays interacting with Earth's atmosphere and thus produces, most importantly for us, the down-going muons.

5.1.2 Neutrino Generators

`NUSIM` [77] is the older of two neutrino generators. It generates a flux of signal muon and electron neutrinos and propagates them through the Earth with random neutral and charged current interactions. Close to the detector, a charged current interaction is simulated. Different energy spectra are obtained by applying weights to the events. However, the scattering angle between neutrino and lepton is always zero with this software.

As documentation [31] is sparse, it shall be noted here that NUSIM shows a technical bug which has to be avoided: With run numbers above 100,000 and 10 k events per run (or with run numbers above 10,000 and 100 k events per run), some random number generator of the software fails and produces non physical output [30]. So if you use NUSIM in the Simuperl framework, always start with run numbers from zero.

Anyway, `NUSIM` is being replaced by the *All Neutrino Interaction Generator* `ANIS` [39, 59]. `ANIS` has finer models for the cross sections, a better modeling of Earth, and it can propagate neutrinos of all flavors up to energies of ZeV. It also correctly simulates the scattering angle between neutrino and lepton.

5.1.3 Muon Propagator

Once up- or down-going muons are generated, they have to be propagated through the ice. The code that does this within the `Simuperl` simulation chain is called `MMC` [28, 27], short for *Muon Monte Carlo*. It simulates the continuous ionization energy loss as well as the stochastic processes of e^+e^- pair production, bremsstrahlung and photo-nuclear reactions (like the production of knock-on (δ) electrons).

5.1.4 Cherenkov Photon Propagators

It would be much too time consuming to propagate each Cherenkov photon through the ice individually. Instead, this is just done once, and as result of the simulation the mean expected number of photons is stored in *tables* as a function of various geometry parameters. Looking up this number in the tables is much faster than calculating it new each time.

For the standard simulation, the established software to calculate the tables is `PTD` (*Photon Transport and Detection*) [55, 56]. This software calculates the expected number of photons as a function of the relative orientation of the optical module to the muon track and as a function of the residual time, that is, the time the scattered photon is delayed compared to an unscattered photon. Only homogeneous ice with average absorption- and scattering lengths can be simulated. However the ice parameters may be different for each optical module.

Various ice models that can be used with `PTD` exist [101]. The simplest model would be a bulk model where all properties are completely averaged, the most current model being `bulkmam`. To do better, it *is* possible to include

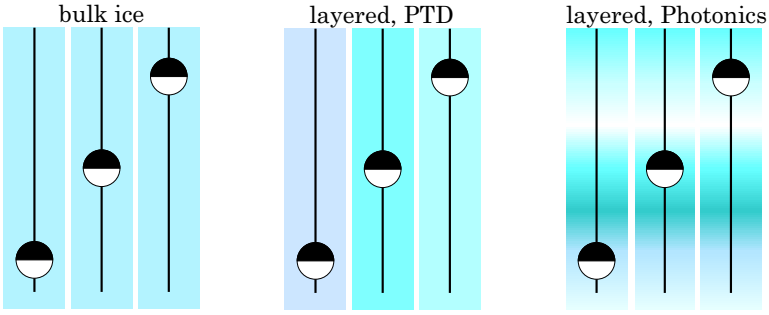

Figure 5.1: A visualization for the three different approaches to implement varying ice parameters in AMANDA simulation. Left: a bulk ice model contains no layered information, the ice is homogeneous for optical modules at varying depths. Middle: In `PTD` it is possible to use an approximation as sketched: For each optical module different ice parameters are used corresponding to the module's depth. However the software still propagates photons through ice with homogeneous properties. Right: With `Photonics` it is now possible to properly simulate the complete layered structure of the ice.

some layered structure in a `PTD` ice model. Figure 5.1 illustrates how this is done: For each optical module one uses bulk ice, but the parameters of this bulk ice can vary from module to module. The most current layered model is `mamint` [46]. Other ice models are hardly used anymore.

However, even with the layered ice model and `PTD` it is not possible to fully simulate the whole wealth of event topologies. A certain class of events, called $\mathrm{CoG_z}$-*events* (which will be investigated in later sections), is observed in the data but not in our simulations. Previous investigations [58] hint that this may be due to an incomplete simulation of ice properties. A much more accurate Cherenkov photon propagator is called `Photonics`, which is introduced in chapter 8. There it is also examined whether or not the conjecture that $\mathrm{CoG_z}$ events are solely caused by the ice properties is true — or whether it is not.

5.1.5 Detector Response Simulator

The simulation software for the detector itself is called `AMASIM` [50]. For each Cherenkov photon `AMASIM` looks up the number of expected photons in the Cherenkov photon propagator's tables, and translates this in a simulated electrical signal. Also, this software considers time jitter that occurs within the photomultiplier tube, it considers dispersion and time delay introduced by the long cables to the surface, and of course it also simulates the implemented triggers.

5.2 Reconstruction Software

An event is a set of pulse and time information that fulfills a trigger condition. The most important trigger is a 24fold coincidence. The event may either be a real data event or a software generated Monte Carlo event. In either case, it is the task of the reconstruction software to deduce the relevant original physics parameters from the recorded information, namely the kind of the particle, its direction and its energy. The handling of the `f2k`-files for this task is done by the `Datahandler` [5] which shoves them through the AMANDA reconstruction software called `Sieglinde` [92].

All events that trigger the detector are summarized in *trigger level*. After some hit cleaning like the removal of noisy optical modules, the sample is referred to as the set of *minimum bias* events. No cuts are applied to this set. But elaborate reconstruction algorithms can be very time consuming, so it is necessary to apply cuts to the event sample (e.g. a cut on the zenith angle) before these algorithms are applied. The subsets that are produced by such cuts are referred to as *level 1*, *level 2* etc. and the definition of these levels varies from analysis to analysis. Eventually, the events that remain in the *final level* set of an analysis is signal dominated.

Various fits and parameters are reconstructed from the available information in order to obtain a measure of the event's quality. This allows to define the cuts which lead to the final level event sample. Some parameters which are relevant for this thesis are introduced here. These and many more may also be found in the literature [12, 20].

5.2.1 Number of Channels and Number of Hits

An obvious quantity to be extracted is the number of hit channels `Nch`, that is, the total number of optical modules that have at least one hit within the readout time window. The number of hits `Nhit` is the number of times that the TDCs go above threshold within the readout time window. It is obviously *not* a measurement of the number of photons that hit the optical modules but instead gives a rough idea about the event's brightness. `Nhit` is important mainly for analyses of extremely high energy events like the search for magnetic monopoles.

5.2.2 Direct Walk

It is important to have a very fast algorithm that gives a first estimate of the track direction. This may be used to cut away down-going muons so that one can use more time-consuming reconstruction algorithms on the remaining events. One such *first-guess* algorithm is the *Direct Walk*, which makes use of the fact that hits close to a track are mainly from unscattered photons. It is a fast algorithm that gives a good first estimate of the muon's direction which can be used as a seed for more time consuming fits.

The vector between each two hits is selected as a preliminary track candidate if the hits are more than $r = 50\,\mathrm{m}$ apart but occur within a time Δt

satisfying

$$\left|\Delta t - \frac{r}{c_{\text{ice}}}\right| < 30\,\text{ns}. \tag{5.1}$$

In other words, the time residuals of the hits have to be small given the preliminary track hypothesis. Each of these track directions defines a cone with an opening angle of 15°. The Direct Walk track is the track that embraces the most track hypotheses within its cone.

5.2.3 Tensor of Inertia

The *Tensor of Inertia* is another first-guess approximation to the muon track. One can get a feeling about the event topology using a mechanical picture. The amplitude of a hit plays the role of a mass at the position of the optical module, and all hits together form a virtual, discrete mass distribution. For this distribution one defines a tensor of inertia I in analogy to the mechanical tensor as

$$I_{m,n} := \sum_{i=1}^{\text{Nch}} (A_i)^w \left(\delta_{m,n}(\vec{r}_i)^2 - r_{i,m} r_{i,n}\right) \tag{5.2}$$

where $\vec{r}_i$ is the position of the optical module that got the ith hit with amplitude A_i. This amplitude may be raised to the weight w, or the amplitude information may be ignored by setting $w = 0$. The eigenvector of the tensor approximates the direction of the muon.

From the mechanical picture another feature is extracted which is of some importance to this work. The *center of gravity* (CoG) is defined as

$$\text{CoG} := \sum_{i=1}^{\text{Nch}} A_i^w \vec{r}_i \tag{5.3}$$

where, again, the amplitude information A_i may be used or ignored by setting the weight w to 0 or 1. In our cases, $w = 0$, and special attention is drawn to the z-coordinate of the center of gravity, CoG_z for short.

5.2.4 JAMS

JAMS (*Just Another Muon Search*) is a cluster search algorithm [93]. The algorithm rotates the coordinate system so that the z-axis is aligned with one out of 48 given equally distributed directions. It calculates a time $t' = z - ct$ for each hit and projects the event onto a t'–x–y–hyperplane. A cluster search is performed in this hyperplane, and the hit with the most neighbors (the cluster center) becomes the center of gravity of the track hypothesis. For all 48 tested directions a least square fit results in an improved estimate of the true track direction. Finally a neural network picks the best track out of these 48 track hypotheses. JAMS is a particularly powerful algorithm to identify coincident muons.

5.2.5 Pandel

The *patched Pandel fit* is a more precise fit algorithm, but it requires more computation time than the above mentioned. It also asks for a few theoretical considerations. The *residual time* Δt is defined as the difference between the recorded arrival time of the photon t_{hit} and the time $t_{\text{geo}} = r/c_{\text{ice}}$ at which one would expect a Cherenkov photon to arrive in the absence of scattering, having travelled a distance r from the muon to the optical module:

$$\Delta t := t_{\text{hit}} - t_{\text{geo}} = t_{\text{hit}} - \frac{r}{c_{\text{ice}}}. \tag{5.4}$$

In the case of an isotropic, monochromatic light source, the distribution of photon arrival times is expected to follow the so-called *Pandel*-function P_{Pandel} [82], which has just recently been extended to include more realistic circumstances [53]. In the simplest case,

$$P_{Pandel}(\Delta t, r) = \mathcal{N}(r) \left(\frac{\Delta t}{\tau}\right)^{\frac{r}{\rho}-1} \frac{1}{\Gamma(\frac{r}{\rho})} \exp\left(-\frac{\Delta t}{\tau} - \frac{c_{\text{ice}}\Delta t - r}{\lambda_a}\right) \tag{5.5}$$

where τ and ρ have to be determined from simulation, λ_a is the absorption length of the ice, and $\mathcal{N}$ is a normalization constant

$$\mathcal{N}(r) = \tau e^{r/\lambda_a} \left(1 + \frac{c_{\text{ice}}\tau}{\lambda_a}\right)^{r/\rho}. \tag{5.6}$$

Typical values are $\tau = 557\,\text{ns}$, $\rho = 33.3\,\text{m}$ and $\lambda_a = 98\,\text{m}$ [12].

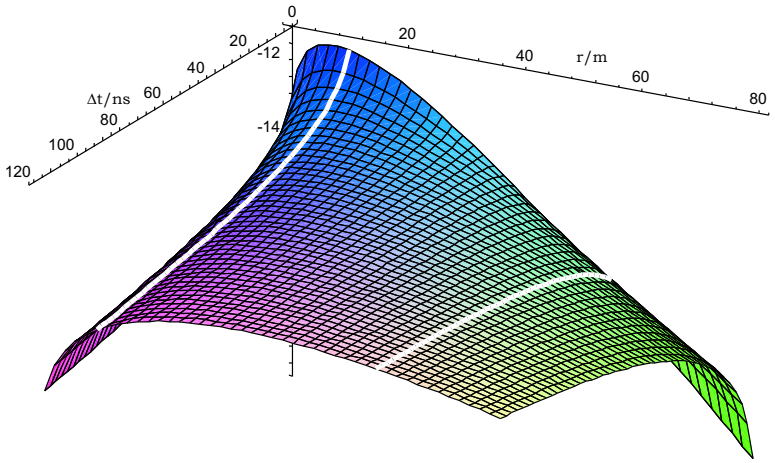

Figure 5.2: The probability to observe a residual time Δt for a photon, arriving from a source at a distance r, is given by the Pandel function 5.5. Here, $\tau = 557\,\text{ns}$, $\rho = 33.3\,\text{m}$, $\lambda_a = 98\,\text{m}$ and the function is plotted in logarithmic, relative units. Slices at constant distances considerably change their shape as indicated by the white lines.

To include time jitter of the photomultiplier, the Pandel function would have to be folded with a Gaussian. However, to make numerical handling

easier, the Pandel function is extended to negative times $\Delta t < 0$ with a Gaussian patch, for times $t \gg \Delta t$ it is left as is, and in between it is replaced by a third order polynomial interpolation. The result is then called the *UPandel* function $\hat{P}_{Pandel}$.

Given the full information of an event, one can now reconstruct the Pandel track. For this, the time residuals Δt are calculated, and one maximizes the Pandel likelihood for varying track hypotheses. For technical reasons, one minimizes the negative logarithm of the individual Pandel likelihoods, that is, one minimizes the function

$$\mathcal{L} := -\sum_{i=1}^{\text{Nhit}} \log\Big(P_{Pandel}(\vec{r}_i, \Delta t_i)\Big). \tag{5.7}$$

The parameters where $\mathcal{L}$ is minimal then give the best guess for the track.

5.2.6 Smoothness

The *smoothness* quality parameter gives an idea about the distribution of hits along the track. To calculate the smoothness, one walks along the reconstructed muon track looking around at right angles from the track. Thus the line of sight sweeps over the hits. One calculates at each step the difference between the distance l_n walked along the track and the hits n seen so far. Both values are normalized to the total track length L and the total number of hits `Nhit`, respectively. The smoothness is then simply the maximum value of this difference that occurs anywhere along the track:

$$\text{smoothness} := \max_n \left\{ \frac{n-1}{\text{Nhit}-1} - \frac{l_n}{L} \right\} \tag{5.8}$$

Very nice muon tracks have a smoothness close to 0, where badly reconstructed events or weird background events like the one in figure 4.8 have a smoothness approaching ± 1. The smoothness idea is extended to account for the asymmetry and inhomogeneity of the AMANDA detector by taking into account the actual probabilities of the hits to occur at a given distance [10]. This parameter is then sometimes abbreviated `S_phit` or `Phit_s`. A technical detail shall be noted, namely, that the smoothness is set to zero for tracks where the algorithm fails. Thus, a cut on the smoothness parameter will always exclude tracks with zero smoothness as well.

5.2.7 Resolution

The pointing accuracy of the AMANDA detector is not only limited by the intrinsic scattering angle between neutrino and muon, but also by the quality of the reconstructed track itself. A measure of this accuracy is a quality parameter called *resolution of the paraboloid fit* [80] which is based on some likelihood reconstruction, Pandel for example. The error in both the azimuth and the zenith angle is estimated for this fit simply by allowing the likelihood to drop to 0.5. Together these two errors form the two half axes

of an error ellipse. The resolution estimator is then either the square root of the area of this ellipse or its average radius. It estimates very well the reconstruction quality of the event. Investigations show that mis-reconstructed tracks usually have a much worse resolution parameters, too.

Part II

This Endeavor

Chapter 6

Angular and Temporal Correlations

Intent: The Zeuthen group has separated a sample of 3369 neutrino candidate events. First investigations did not reveal any obvious contributions from extraterrestrial sources, but instead the sample is compatible with the hypothesis that all events stem from the background of up-going atmospheric neutrinos. But does this sample show any significant excesses when the timing information is also used? Or are there angular correlations hidden in the sample?

Organization: Section 6.1 introduces the final event sample. In section 6.2 I do a simple search for correlations in time and in section 6.3 I search for correlations in both time and angle together.

6.1 The Sample

The Zeuthen group has produced a high quality sample of neutrino candidate events, based on the combined 2000-2003 AMANDA raw data with a live-time of 807 days [3]. A sample of 3369 up-going events was selected out of more than $7 \cdot 10^9$ events. The result of this sophisticated analysis is shown in figures 6.1 and 6.2. The sensitivity of this analysis is much better than previously published results [4, 13].

No obvious excesses were found in the sample which is compatible with the assumption that it consist purely of atmospheric neutrinos (*background hypothesis*). Tests where done on this sample to put the background hypothesis through its paces. A search for an excess in a binned search of the full northern sky was performed as well as the search for an excess near candidate sources [3]. A search for possible angular correlations of the events yielded no significant effect [25, 61]. Some other tests are described below.

6.2 Correlations in Time

An outburst of neutrino events could show up in the time distribution of the events. The 3369 events occurred during a lifetime of 807 days, which gives

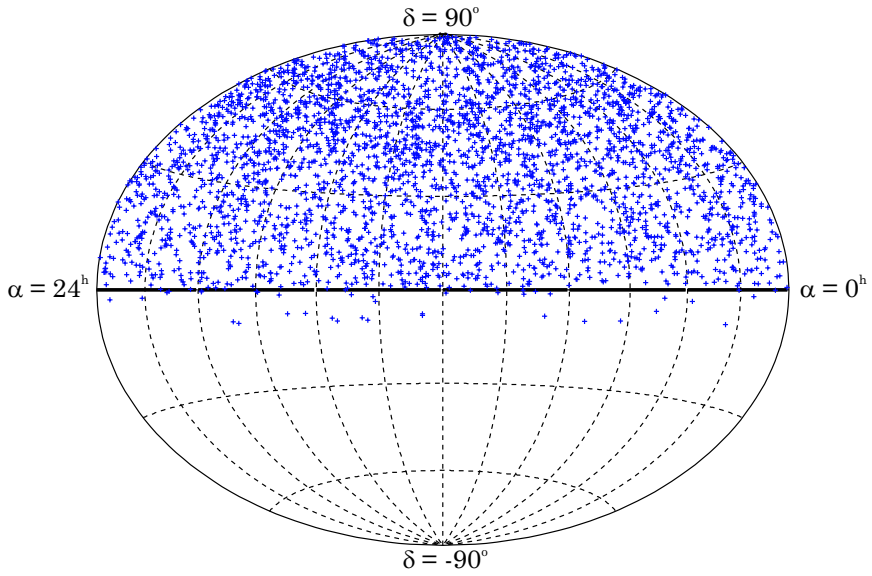

Figure 6.1: The AMANDA neutrino sky: A plot of our 3369 neutrino candidates [3]. The projected origins of these events show a uniform coverage of the northern sky.

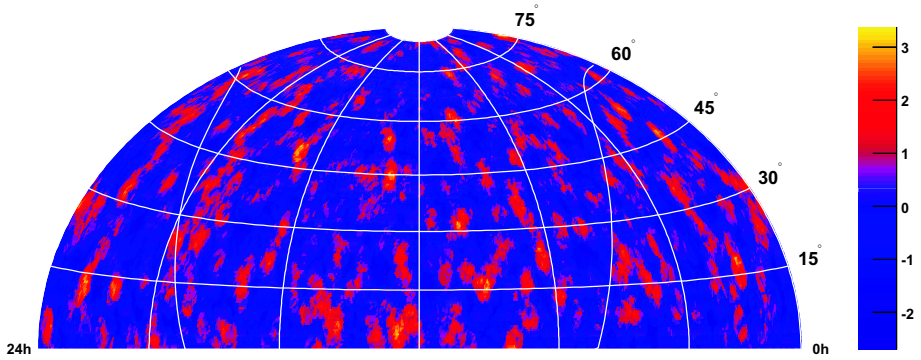

Figure 6.2: The significance map of the AMANDA neutrino sky for the events collected between 2000 and 2003. Although some areas have excesses with significances larger than 3σ, this is not enough for a detection. The reason for this is the *trial factor*, namely, that in maps with this many bins one always expects such (or even higher) excesses [3]. Thus the map is not indicative of point sources but is compatible with background.

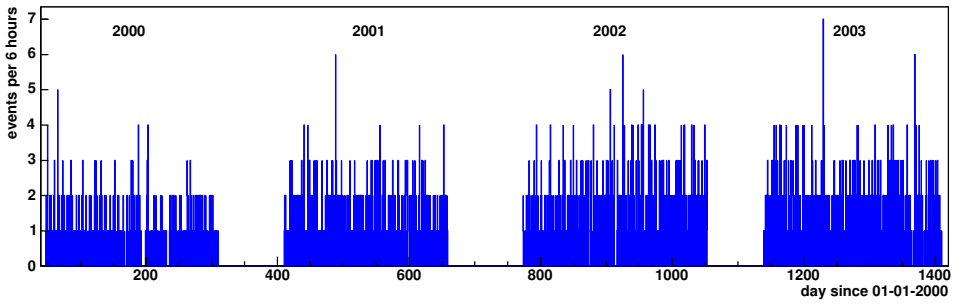

Figure 6.3: A time-line of the neutrino events. On average, every 6 hours an event is expected. The histogram shows the different years 2000 through 2003. The gaps in between are periods where data is not used for this analysis due to increased maintenance of the detector in the Antarctic summer season. After 2000 and after 2001, the AMANDA trigger rate increased following some improvements of the detector electronics. This pervades through all data reduction levels, so there are more neutrino events after the year 2000.

on average 0.17 events per hour or one event every $\approx$ 6 hours. However, my investigation of the sample on various timescales did not result in any significant pattern. One of the highest concentrations is 4 events within 47 minutes which occurred on May 14th, 2003 (highest peak in figure 6.3). At first sight, this sounds indicative. However, the chance probability for this was found with a simple Monte Carlo to be around 14%, since the events are not correlated in space angle. So this is compatible with the background hypothesis as well.

6.3 Search for Doublets

Both angular and temporal correlations can be searched for together. I define a *doublet* simply as two events that are close in time and angle. Transient neutrino point sources may show up in the distribution of doublets. Reasonable values for the event separations are anything above $\approx 2^\circ$, the angular resolution of the AMANDA detector. For temporal separations, the lower limit investigated is one minute, going up to separations of 12 hours and one week.

The number of doublets for given angular and temporal separation was tested against a background sample, obtained by randomly interchanging the true arrival times and right ascensions of the events. This procedure correctly simulates the azimuthal detector acceptance as well as the detector live-time. As can be seen from figures 6.4 and 6.5, no strong excesses were found for a variety of search parameter settings. The observed number of doublets lie mostly within the 1σ error bars.

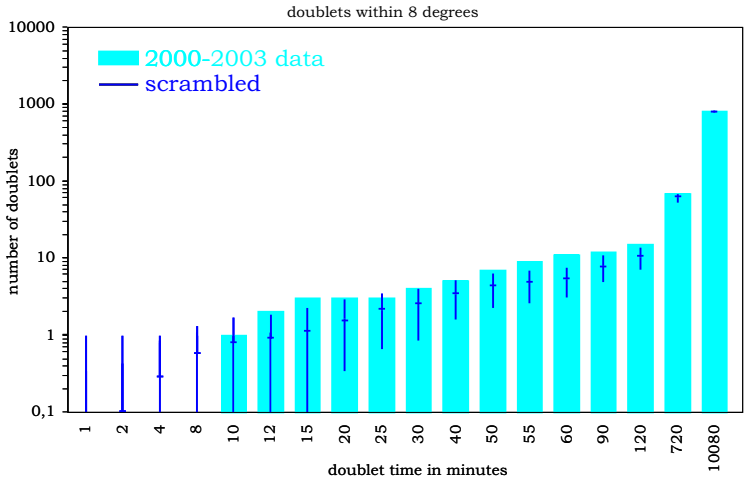

Figure 6.4: Number of doublets occurring within a maximum angular separation of 8° and within various maximum time differences. The times where chosen following no particular pattern, the last bins are 12 hours and 1 week. The doublet numbers from the 2000-2003 neutrino sample are shown in light blue. By scrambling arrival times and directions, the dark blue values are obtained, shown with 1σ error bars as inferred from the simple simulation. They represent the expectation from a statistical background. All observations are within or close to this range.

6.4 Conclusion

Searches for temporal or angular correlations in the AMANDA 2000–2003 point source sample show no conclusive evidence for contributions from extraterrestrial point sources. The time distribution of the events is compatible with a random sample. Also no excesses of doublets with varying temporal and angular cuts were found in the sample.

Tonio Hauschildt discussed already in his thesis [42] the limitations of AMANDA point source searches which even more apply to this sample: The statistical fluctuations of the 2000–2003 point source sample are smaller than the fluctuations that are expected from systematic errors. Thus simply adding data from 2004 to the sample will not significantly improve its impact in the time integrated search for neutrino point sources. Instead of investigating the existing sample in even more detail, I tackle the most important questions of systematic uncertainties in the remainder of this thesis.

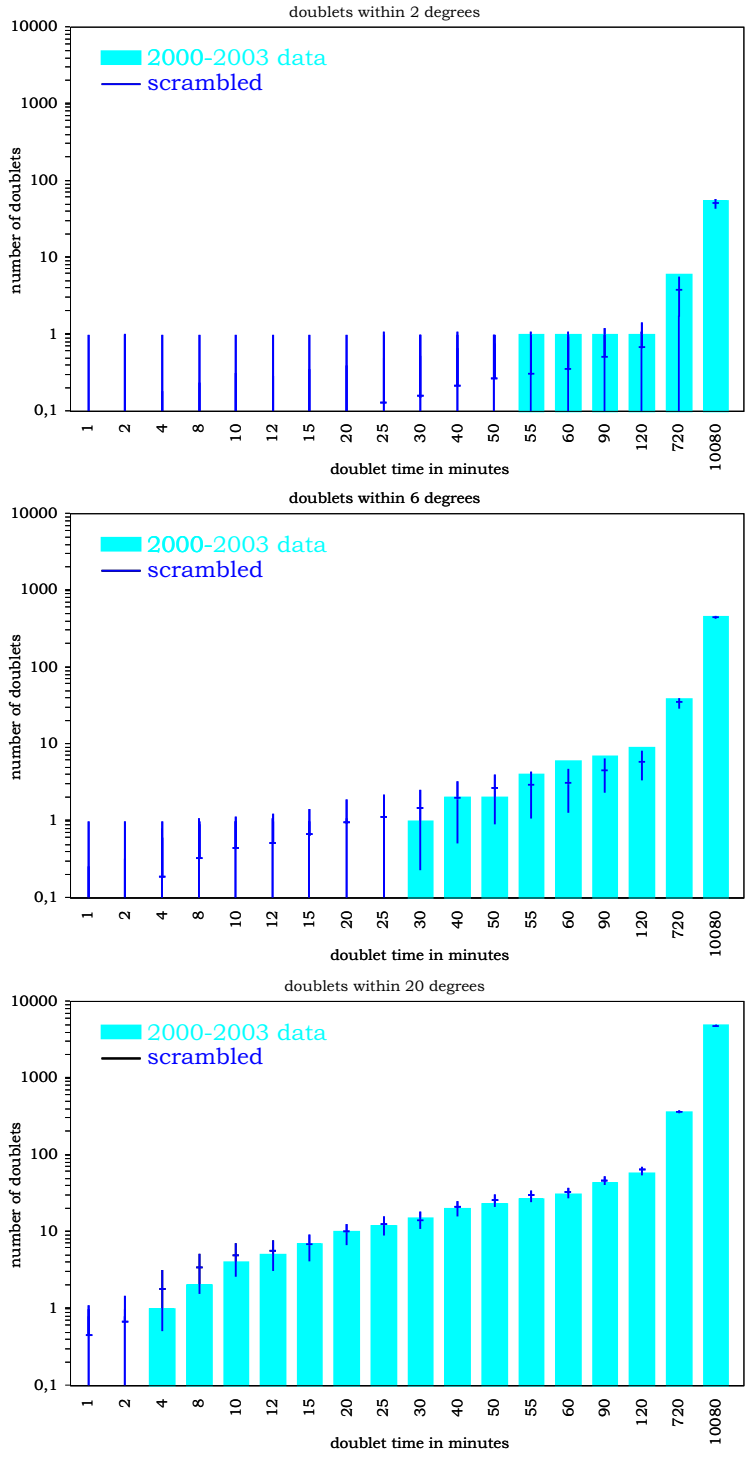

Figure 6.5: Some more doublet distributions. Again all numbers from the data sample, plotted in light blue, are well withing the expectations from a pure background sample, plotted in dark blue together with the 1σ error bars.

Chapter 7

Detector Uptime

Intent: Is AMANDA taking data constantly through the day? The distribution of *final level* events is uniform throughout the day. But collaborator Andreas Gross investigated the outcome of his point source stacking analysis together with Markus Ackermann and found an indication that the events in the sample may not be evenly distributed in right ascension. This is the starting point to this analysis. To see where the effect is coming from, I went to more and more basic levels. The results are presented here.

Organization: Section 7.1 introduces the effect. In section 7.2 a likely explanation is derived which is supported in section 7.3.

7.1 Events in the Course of the Day

Figure 7.1 shows the arrival times of the 3369 neutrino candidate events. Within the statistical errors they occur uniformly distributed throughout the day. However, things look very different if we do not apply any quality cuts to the events, that is, if we go back to *minimum bias* data, as shown in figure 7.2: Clearly the distributions are not flat but show a variation at the 1% level. It is the purpose of this chapter to explain the origin of this effect.

Any effect related to station life is expected to show up when plotted against Greenwich Mean Time (GMT), as the wall-clocks at the Amundsen-Scott South Pole station are set to New Zealand Time (NZT), which is just GMT plus 12 hours. Effects of astronomical origin on the other hand are expected to show up when plotted against the Sidereal Time, which measures a day with respect to the fixed stars rather than the Sun.

A distinction has to be made between what I call *winter* and *summer* time: The detector is maintained during the Antarctic summer months when staff and equipment can be flown to the South Pole. The detector performance is usually quite irregular during this time, so the corresponding runs are excluded from usual physics analysis. This is already clear from figure 6.3 in the previous chapter which shows clear gaps in between the years. The remaining $\approx 3/4$ of the year are referred to as *winter* months.

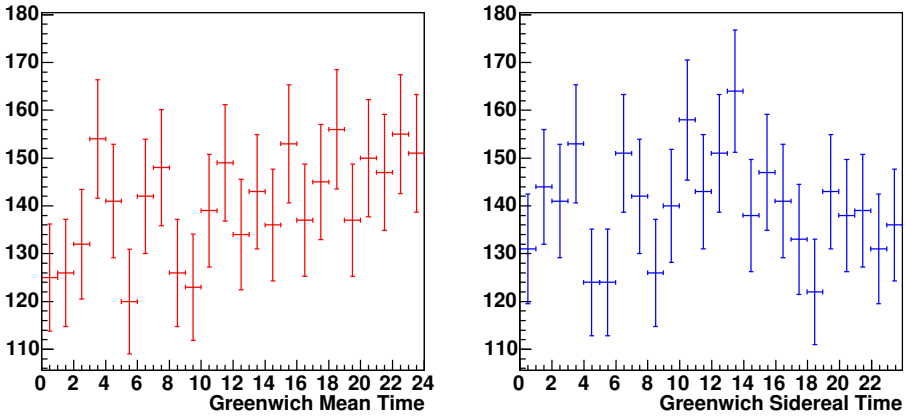

Figure 7.1: The arrival times of the 3369 final events. The histograms in this chapter are all divided into 24 one-hour bins, plotted on the left side against Greenwich Mean Time (GMT) in red, and on the right against Greenwich Sidereal Time (GST) in blue. The error bars are the $\sqrt{N}$ errors from an assumed Poisson distribution. No significant variation through the day is obvious on this final level.

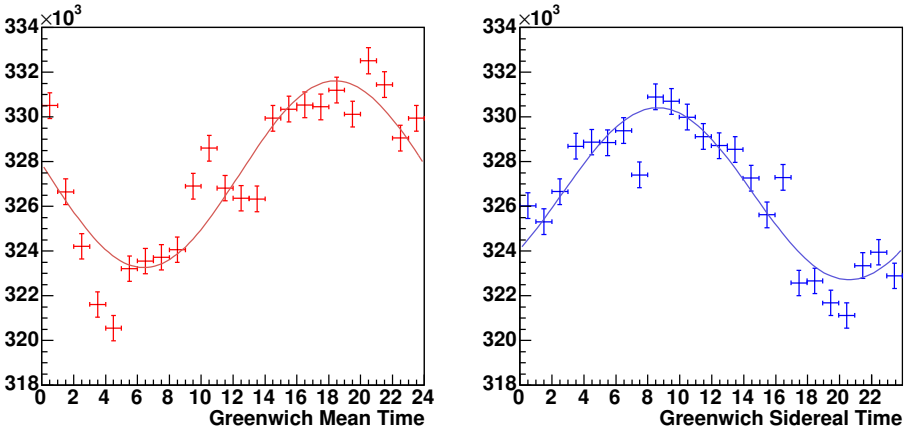

Figure 7.2: The arrival times of almost 8 Million minimum bias *winter* events vary significantly throughout the day. Sine functions with given one-day-periods (solar or sidereal, respectively) are fitted. The amplitude of the variation is $(1.3 \pm 0.1)\%$ in the GMT curve and $(1.2 \pm 0.1)\%$ in the GST curve. As only *winter* days are considered, covering less than 3/4 of a year, a variation in GMT does not necessarily smear out in sidereal time.

It is important that AMANDA has a uniform coverage over sidereal time. This is implicitly used in most blind analyses as one interchanges (*scrambles*) the right ascension of the events. The underlying assumption is that our distributions are uniform in right ascension, so the blue plots in this chapter should always be flat.

Sinusoidal functions with periods of one solar day (in the case of the GMT histogram) or one sidereal day (for the GST histogram) are fitted, see figure 7.2. The amplitude of the effect is inferred from these fits to be just above 1%. Though small when compared to other systematic effects within AMANDA, it deserves some attention.

7.2 Starting Times of Files

AMANDA events are written to *files*, first binary files at the pole, and later `ASCII`-Files in the so-called `f2k`-format. One file typically spans about 10 minutes of detection time. Many such files combined form a *run* which, if everything goes well, lasts a day.

To check whether the above mentioned effect could stem from detector operation, I looked at the distribution of files throughout the day. As files last only about 8–12 minutes and are never much longer or shorter, it is justified to simply plot the starting times of files. The information for this is taken from the `Datahandler`'s log file. Figure 7.3 shows the distributions.

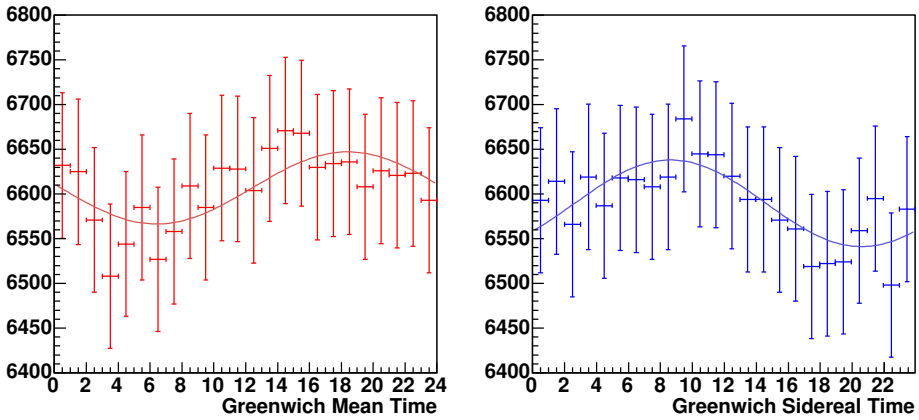

Figure 7.3: Distribution of starting times of the f2k *winter* files. Again, the years 2000–2003 are plotted together, and sine functions are fitted. Here, both wavelength (a solar or sidereal day) and phase (as in figure 7.2) are fixed. The amplitudes of the fits are only $(0.6 \pm 0.4)\%$ for the GMT curve and $(0.7 \pm 0.4)\%$ for the GST curve. Within the errors, it is thus just possible to explain the effect observed in the event histograms 7.2.

To both curves sine functions are fitted, this time with both the periods and phases fixed to these from the previous fits. Although a flat distribution

is also possible within the error bars, this procedure is well motivated: The question is whether a possible sinusoidal variation could explain the observed effect in figure 7.2.

The amplitudes in figure 7.3 are fitted to be just below 1%. Taking into account the rather large errors of the fits, this may explain the observed event variation. Thus the variation of the event rate stems not from a true physics effect, but from the detector uptime, which is not uniformly distributed through the day. (The joke goes that the winter-overs work hard, maintaining the detector throughout the whole polar night — except around dinner time where they take a break no matter what. Thus the dip around 6 pm New Zealand Time.)

7.3 So what about the Event Rates?

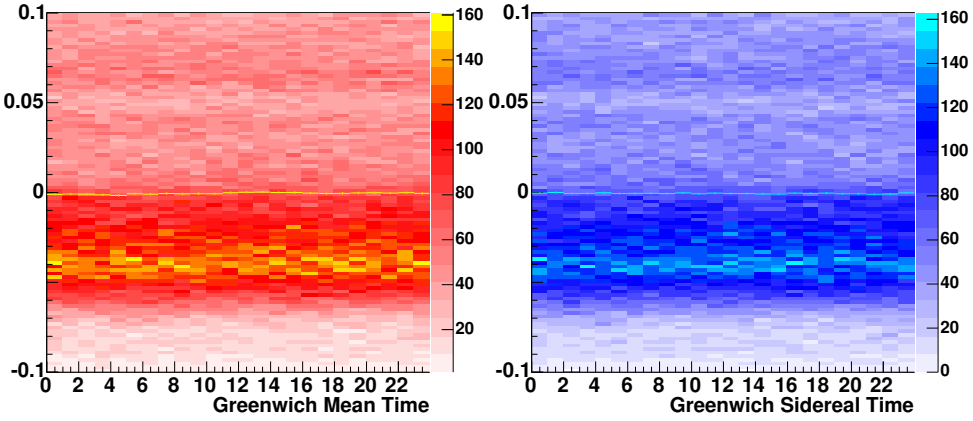

Figure 7.4: A physics effect should show up most significantly in the event rate. These plots show the event rate relative to the yearly average (the ordinate showing relative units). The average trigger rates vary for the different years and go up from about 45 Hz in 2000 to about 64 Hz in 2003 due to an improved detector performance. To compare the different years in a single plot, the trigger rate of each file was normalized to the average trigger rate of that year, and 1 subtracted. The curve is flat by all means. The yellow respectively blue line shows the mean of the trigger rate which is flat to an accuracy better than 0.02%

To increase the reader's satisfaction with this very earthly explanation, figure 7.4 shows a combined two-dimensional histogram (colored rectangles) with a profile plot (lines) of the event rates per file, i.e. the trigger rate averaged over all 2000–2003 *winter* files. A true physics effect should show up in the event rate, but the distributions are both flat.

In addition, similar plots like the `Nch` weighted distribution were investigated and were all found to be flat to better than $\approx 0.1\%$. So the explanation given above may explain the observed effect.

7.4 Conclusion

The solar and sidereal event distributions of AMANDA data are not uniform but show a variation on the 1% level. This seems not to be a true physics effect since the event rates indeed are uniform. A likely explanation for the variation has been given, namely, that the detector uptime is not distributed uniformly throughout the day. This very technical effect then pulls through the analysis chain. Still 1% is neglible compared to other systematic effects, and the following chapters will investigate more pronounced uncertainties.

Chapter 8

Advanced Glacier Modeling

Intent: Processing AMANDA data we observe a class of events dubbed CoG_z events which previously could not be modeled with adequate accuracy. The conjecture was that an improved modeling of the layered ice structure would be able to reproduce this class of events in the simulation. To this end, the new software `Photonics` is able to simulate the full depth-dependence of the AMANDA ice. A script was written by the author to implement `Photonics` in the simulation chain `Simuperl`. This allowed a first simulation run using the new ice modeling. Although the `Photonics` version that was available for this thesis contained some bugs, the above conjecture is tested.

Organization: Section 8.1 introduces the CoG_z events, and section 8.2 the `Photonics` software. In section 8.3 the script that implements `Photonics` into the simulation chain is explained. Section 8.4 then shows first results with the new simulation.

8.1 CoG_z Events

The standard AMANDA simulation is capable of describing the data to a high level of accuracy. However, a certain class of events, the so-called CoG_z events, were previously not fully understood. Figure 8.1 shows a plot of 2002 data on minimum bias level, i.e. no quality cuts are applied. The z-coordinate of the center of gravity (CoG_z) is plotted in relative detector coordinates, where the detector center at $z = 0$ lies at a depth of 1730 m. The plotted zenith angle is reconstructed using the Pandel algorithm. The events with reconstructed zenith angles greater than $\approx 80°$ show a distinct layered structure, peaked around -100 m (at a depth of 1830 m), 40 m (1690 m) and 180 m (1550 m).

It was quickly noted that the more densely populated depths correspond to ice layers with little absorption, and that these events actually were down-going muons mis-reconstructed as up-going [58]. Light propagates further in these layers, so events get distorted in a way that was not simulated. The reconstruction software could not be improved due to the missing simulation. Luckily, CoG_z events generally show bad quality parameters, like high smoothness values for example. Therefore the events drop out of the

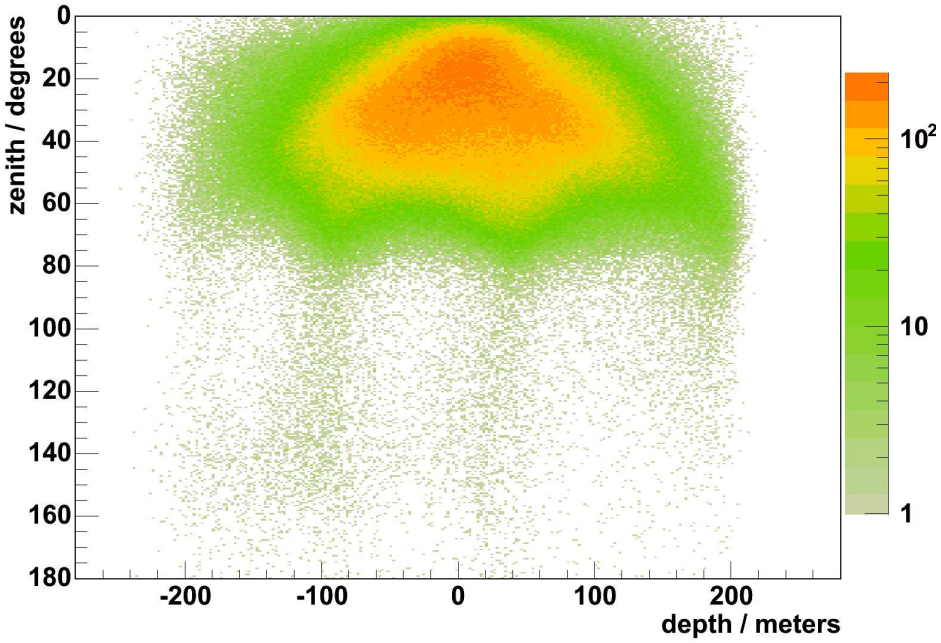

Figure 8.1: A plot of the z-coordinate of the center of gravity (CoG_z) from over 10^6 minimum bias events that occurred during 2002. The depth is given in relative detector coordinates, zero corresponds to a depth of 1730 m. Almost all events are down-going muons. Above horizon ($0° < \theta < 90°$) the distribution reflects the strong zenith angle dependent acceptance of the detector. In the important signal region below horizon ($90° < \theta < 180°$) the figure shows a distinctive layered structure. The three accumulations coincide with layers of highly transparent ice.

higher reconstruction levels and do not prevent point source searches. In the case of the four-years point source sample (investigated in chapter 6) the contamination with mis-reconstructed events is less than 10%.

However, the true nature of the CoG_z events remains unresolved. The comparison of the reconstructed Pandel zenith angle from a large `dCorsika` simulation with data in figure 8.2 shows very good agreement above horizon ($\theta < 90°$), but considerable disagreement below horizon. Two major steps to improve this agreement are the main outcome of this thesis.

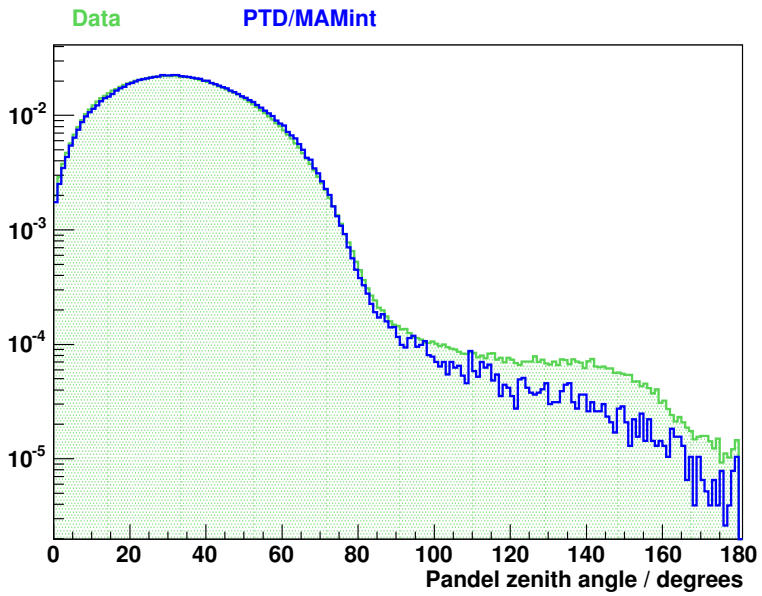

Figure 8.2: A comparison of data and simulation. The reconstructed Pandel zenith is plotted for both 2002 data in green and a large `dCorsika` simulation of atmospheric muons using `PTD` with the `mamint` ice model in blue. Both distributions are normalized to unity. Above horizon the distributions agree to a very high precision, but below, they strongly disagree. Note the logarithmic scale of the plot.

Unsimulated features have to contribute in this region. Such unsimulated features are coincident muons (like the one in figure 4.8 on page 36), and the layered ice structure. Of course, the `dCorsika` simulation does not include atmospheric or extraterrestrial neutrinos either, but their contribution is thought to be negligible at this minimum bias level: Above horizon roughly $2 \cdot 10^9$ events are registered every year, below horizon about 10^6 events. The expectation from atmospheric neutrinos is only about $2 \cdot 10^3$ events per year.

8.2 Advanced Modeling

To increase the understanding of the important signal region below the horizon, the collaboration undertook a big effort to investigate the optical ice properties of the South Pole glacier and set up a detailed simulation package called `Photonics` [75]. With this software, the ice properties are modeled with their full layered structure as inferred from measurements [103]. The photons are simulated following a Cherenkov spectrum, and all wavelength dependencies of the ice (as shown in figure 4.10 on page 39) are included. `Photonics` has only one notable limitation at the moment, namely, that it can only simulate ice layers in the x–y–plane. The assumption that the ice in the vicinity of AMANDA indeed shows such a layered structure is is inferred from our calibration data and additionally supported by images obtained by airborne radar, as shown in figure 8.3. Even for the much larger IceCube detector this assumption holds to good accuracy.

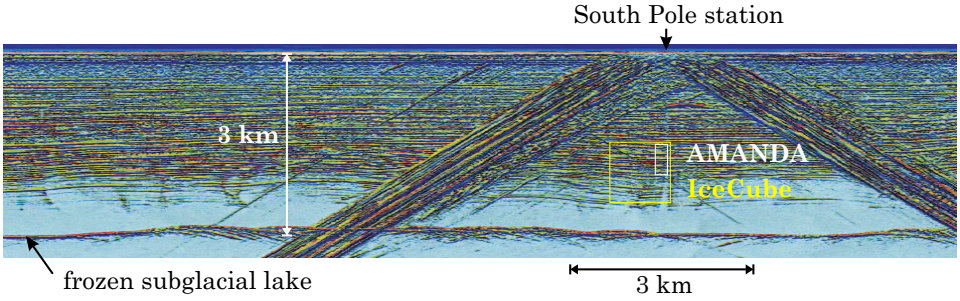

Figure 8.3: An airborne radar image of the South Pole glacier, together with the approximate positions of AMANDA and IceCube. At least for AMANDA the layered-ice-hypothesis is well justified. The strong diagonal structure comes from scattering of radar waves off the South Pole station. Radar image by Blankenship et al. [21]. (AMANDA data suggests that even near the bedrock, temperatures are still below freezing point [85, 86], so the subglacial lake at the left is frozen and a candidate lake to test sterile ice drilling)

Figure 8.4 shows the Cherenkov cone that is emitted by an up-going muon travelling through the detector as simulated with `Photonics`. The different optical properties of the ice introduce a significant distortion of the Cherenkov cone.

`Photonics` stores the photon probability density (dP/dt) and the photon amplitude in *tables* which have six dimensions: three spatial, two directional and one temporal. The coordinate system is not fixed to the detector, but to the particle which emits the light. With the more detailed description, one would like to have a fine binning in all coordinates. In particular, a binning of $\lesssim 10\,\mathrm{m}$ in the depth z is desirable. This results in large tables with many Gigabytes of data. With the available computer technology it is not yet possible to load the whole table set into memory at once.

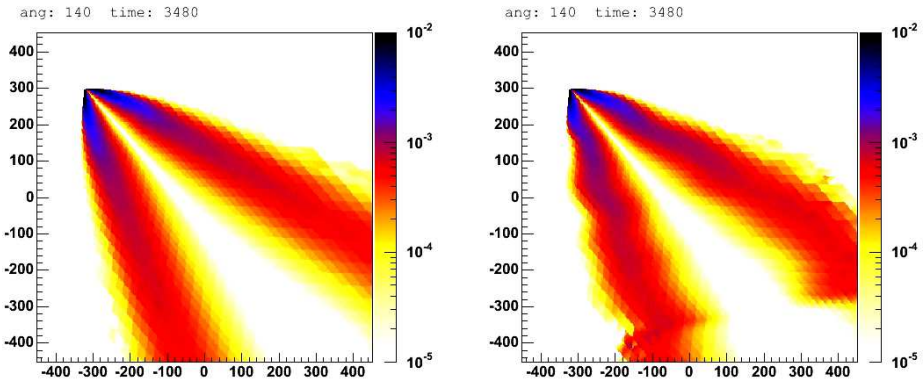

Figure 8.4: The Cherenkov cone as simulated with `Photonics` is visualized by plotting the normalized photon probability density (dP/dt). Left: Using a bulk ice model, the Cherenkov light forms a distinctive Cherenkov cone. Right: Introducing the observed ice layers to the simulation causes the Cherenkov cone to distort. These plots and nifty animations of the travelling muon by Johan Lundberg [69].

8.3 Implementation in the Simulation Framework

To circumvent this problem, I wrote an addition to the `Simuperl` framework that makes use of the coordinate system in the tables. The new script `zenithwise.pl` [60] splits the events zenith band wise before they are processed by `AMASIM`. To process such a subset of events it is no longer necessary to load the full `Photonics` table set into memory, but instead it is enough to load the corresponding tables for the particular zenith band only. Thus the required memory is reduced to that for the tables of a zenith band, typically 1 GB, and this is easily matched by the available computer systems. The `zenithwise.pl` script also handles the individual files, sets up the `Scatserver` [51] for communication with `AMASIM`, merges the files after processing and eventually takes care of file cleanup. The script will be included in the next `Simuperl` release together with some minor modifications of other `Simuperl` scripts that were necessary to make the whole thing go together.

8.4 First Results

With the angular processing of events it is now possible to run an AMANDA simulation using `Photonics`. Figure 8.5 shows the $\mathrm{CoG_z}$-distributions for 2002 data and a `Photonics` simulation. Both samples are cut to *level 3*, meaning that their reconstructed zenith angles are restricted to $> 80°$. More precisely, the requirement is $\theta_{\mathrm{JAMS}} > 80°$ and $\theta_{\mathrm{UPandel}} > 80°$. This is necessary because without cuts the $\mathrm{CoG_z}$ structure would not be visible but swamped by the down-going muons which do not show a layered pattern, compare figure 8.1.

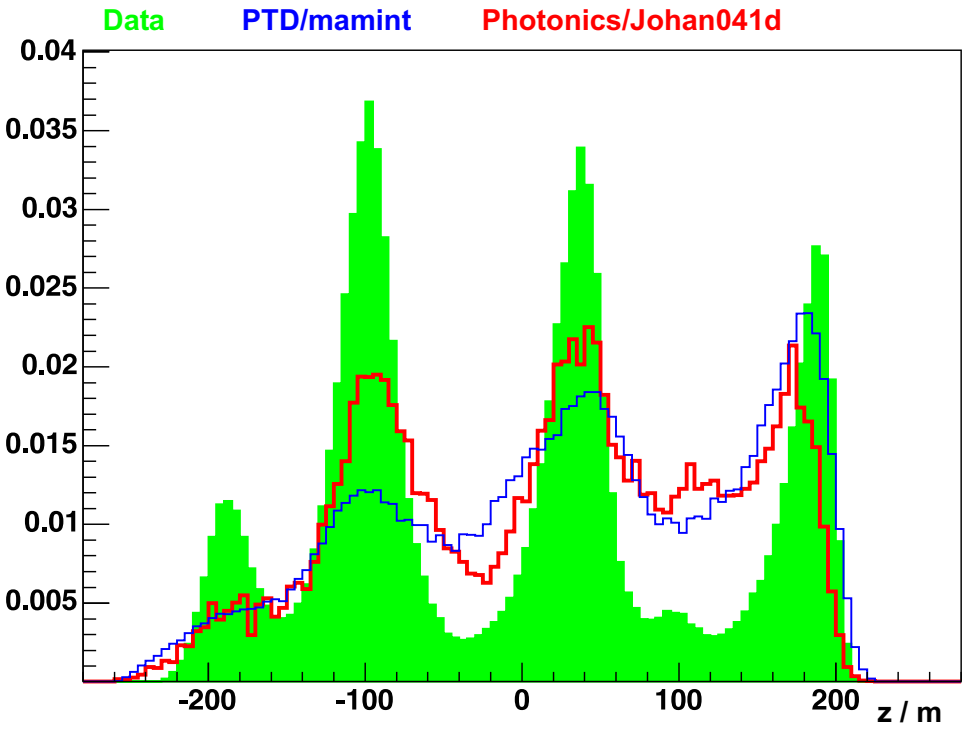

Figure 8.5: A comparison of 2002 data events with the `PTD` and the `Photonics` simulation. Plotted are the Centers of Gravity of events below the horizon (level 3). In green, the data shows the distinctive layered structure. The old `PTD` simulation, shown in blue, is not fully capable of reproducing this structure. The new `Photonics` simulation indeed does much better. Yet it fails to reproduce the sharpness of the data peaks (see also [63]).

As can be seen in figure 8.5, the peaks at $z \approx -100\,\mathrm{m}$ and $z \approx 40\,\mathrm{m}$ are indeed reproduced with the `Photonics` simulation! On the other hand, the `PTD` simulation fails to do so. The peak at the upper end of the detector at $z \approx 200\,\mathrm{m}$ is seen in both `PTD` and `Photonics` simulations. It is caused by muons stopping just above the detector. Such muons yield hits only in the uppermost layer and are therefore mis-reconstructed as horizontal tracks.

Further and more detailed investigations of the `Photonics` simulation showed that some problematic issues were left [62]. For example, the trigger rate was only about 3/4 of the data trigger rate, and test simulations using only stopping muons and no secondary particles would yield no triggered events at all. Eventually a bug concerning starting and stopping muons was identified by our Swedish colleagues. Unfortunately, resolving this problem and implementing the changes into the simulation chain took a long time. The fixed version of `Photonics` and the updated `Scatserver` are finally available, but unfortunately were delivered too late to be considered in this thesis. Therefore no further investigations with `Photonics` are presented.

8.5 Conclusion

The old `PTD` software is not capable of reproducing the CoG_z structure that one observes in the data below the horizon. An advanced ice model can be simulated with the `Photonics` software which produces large tables that can not be loaded into memory at once. Therefore the `Simuperl` simulation chain was patched and an additional script was written that splits the events zenith band wise. Only a subset of the `Photonics` tables has to be used to process the splitted events, so that it is possible to simulate the impact of the advanced ice model with current computers. A first simulation showed that indeed the proper simulation of the complete ice properties improves the agreement of data and simulation. However, the software contained a bug, and the fixed software was not available for this thesis.

Chapter 9

Sensitivities of Optical Modules

Intent: How sensitive are the individual optical modules to incident light? For a given optical module many effects contribute to this parameter, like the transparency of the glass sphere and the light collection efficiency of the photomultiplier. Other dependencies are not accessible in laboratory measurements, such as the properties of *hole ice*. Thus one has to measure the sensitivities in situ. Here, I develop an analysis which uses the abundant down-going muon data. With this method the sensitivities of AMANDA's optical modules are determined.

Organization: Section 9.1 explains the method that will be used. It is necessary to define a sample of muons which is done in section 9.2. The method is tested against the simulation in section 9.3. The results from an application of the method to the detector as of 2001 are presented in section 9.4.

9.1 The Method

9.1.1 Sensitivity

The sensitivity of an optical module is defined as the ratio between detected photons and the photons that hit the module:

$$S_{\text{photon}} = \frac{\text{number of detected photons}}{\text{number of total photons}}. \tag{9.1}$$

This sensitivity already includes effects like the absorption of photons in the glass sphere as well as the quantum efficiency of the photomultiplier. It should be determined for all optical modules.

To cope with systematic uncertainties it is essential to measure the sensitivity in situ. In particular, the optical modules contain an *optical gel* that couples the photomultipliers to the glass sphere both mechanically and optically. The behavior of this gel at low temperatures is unknown. Some observations in freezer laboratories suggest that the optical gel may become milky or get cracks. In addition, air bubbles may get stuck to the glass

spheres during deployment. An in situ measurement includes these uncertainties.

While the number of detected photons in equation 9.1 is accessible in the data, the total number of photons that hit the glass sphere is unknown. As we have seen in the previous chapters, in situ light sources can be used to measure the ice properties. But they do not have a defined light output due to kilometer long glass fibers and uncertain conditions in the ice. Therefore, a different approach has to be followed [72, 73].

9.1.2 Track Sensitivity

In usual AMANDA analyses, down-going muons are a nasty background. The short scattering lengths reduce the accuracy of the detector. Here, I turn this to our advantage by using both features to determine the sensitivities of the optical modules relative to each other.

As long as only *relative* sensitivities are of interest, it is reasonable to define the *track sensitivity* as

$$S_{\text{track}} = \frac{\text{number of detected tracks}}{\text{number of total tracks}}. \tag{9.2}$$

The track sensitivity is the visibility of tracks for a given optical module. In addition to the bare sensitivity S_{photon} (equation 9.1) this track sensitivity includes other parameters as well, like scattering and absorption in ice. In particular the properties of *hole ice* influence S_{track}: The strings that hold the optical modules are deployed by melting holes into the ice. The water in these holes quickly refreezes within a few days. The process introduces air bubbles into the ice which strongly reduce scattering lengths. The formation of the air hydrate clathrates (section 4.4.1 on page 32) is believed to be slow compared to the expected AMANDA life time; the actual optical properties of this hole ice are not known [78].

The nature of the considered tracks also influences S_{track}. In addition, it depends on the distance r of the tracks to the optical module: Less photons will get to the module from tracks that are further away, as light gets absorbed or scattered away. This dependence of $S_{\text{track}}(r)$ was modeled using `PTD` [55]. No analytical expression is given, but for distances larger than approximately one effective scattering length ($\approx 20\,\text{m}$) the simulation is fitted well by a simple exponential. As will be shown shortly, this is consistent with the Pandel treatment [82].

At first, one might think that the track sensitivity at $r = 0$ is a measure of the optical module sensitivity. But this is not true: In the immediate proximity of the optical module, it is likely to see many more than just one photon of each track. As S_{track} is always smaller than 1 by definition, the track sensitivity approaches unity and saturates at this value. This does not allow to estimate the true sensitivity of the optical module. To finally derive the correct quantity that will serve as a measurement of the relative sensitivities of the optical modules, an additional statistics effect has to be considered.

9.1.3 Poisson Statistics

The number of photons arriving at the optical module follows a Poisson distribution

$$P_\lambda(\mathrm{Nhit}) = \frac{\lambda^{\mathrm{Nhit}}\, \mathrm{e}^{-\lambda}}{\mathrm{Nhit!}} \tag{9.3}$$

where λ is the expected number of photons to arrive at the module from a given distance r, so $\lambda = \lambda(r)$ and $P_\lambda(\mathrm{Nhit}) = P_\lambda(\mathrm{Nhit}, r)$. At any given distance r, the difference $1 - S_{\mathrm{track}}$ is the probability that no photons hit the optical module. From equation 9.3 it follows immediately that

$$1 - S_{\mathrm{track}} = P_\lambda(\mathrm{Nhit} = 0, r) \tag{9.4}$$

$$= \mathrm{e}^{-\lambda(r)} \tag{9.5}$$

and thus the number of photons expected to hit the module after being emitted from a track at a given distance is

$$\lambda(r) = \ln\left(\frac{1}{1 - S_{\mathrm{track}}(r)}\right). \tag{9.6}$$

$\lambda(r = 0)$ will serve as a measure of the relative sensitivity of AMANDA's optical modules. However, it is not inferred directly from this equation but from the extrapolation of a fit to S_{track} as explained in the next section.

9.1.4 The Procedure

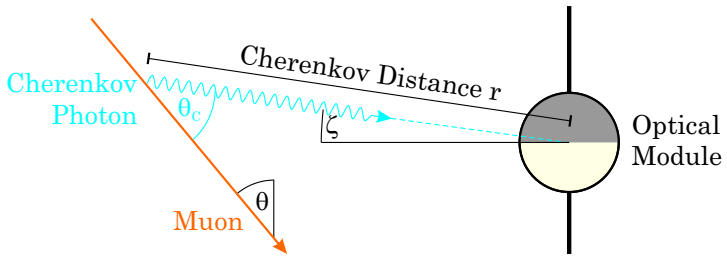

Figure 9.1: The relevant geometry: A down-going muon with zenith angle θ emits a Cherenkov photon at an angle θ_C which hits an optical module under an angle ζ after travelling the (Cherenkov–) distance r.

AMANDA optical modules look downward to optimize the detector for up-going muons. For the majority of Cherenkov photons it is therefore in principle not possible to reach the photomultiplier tube unscattered. Hence the important distance is not the distance of the track to the optical module, but what I call the *Cherenkov distance* r that an unscattered Cherenkov photon would travel. To allow for photons to scatter on their way to detection, an important condition is $r \gtrsim \lambda_{\mathrm{eff}}$, where λ_{eff} is the effective scattering length.

Thus $\lambda(r = 0)$ is not inferred directly. Instead, $\lambda(r)$ is evaluated at various distances. One can obtain the probability P_{getit} that a photon arrives at the optical module after travelling a distance r by integrating the Pandel function (equation 5.5 on page 46) over all times:

$$\begin{aligned} P_{\text{getit}}(r) &= \int_0^\infty P_{\text{Pandel}}(\Delta t, r)\ \mathrm{d}(\Delta t) && (9.7)\\ &= \mathcal{N}_0\, \mathrm{e}^{-r/\lambda_a} \left(1 + \frac{c\tau}{\lambda_a}\right)^{-r/\rho} && (9.8)\\ &= \mathcal{N}_0\, \mathrm{e}^{-br} && (9.9) \end{aligned}$$

where

$$b := \frac{\rho + \lambda_a \ln\left(1 + \frac{c\tau}{\lambda_a}\right)}{\rho\lambda_a}. \qquad (9.10)$$

Thus an exponential e^{a-br} is fitted to $\lambda(r)$ between 20 m (to allow for scattering) and 36 m (so that the statistics are still high). The slope b depends on the ice properties in the vicinity of the optical module. The constant offset a is trivially related to the sensitivity of the optical module: $\lambda(r = 0) = \mathrm{e}^a$.

As it turns out, the fitted slope b scatters strongly for the different optical modules. But the ice properties are the same for each optical module at a given depth. Thus the slope b can be fixed to the average slope $\tilde{b}$ of the corresponding ice layer. Here, the running median of all optical modules within ± 10 m in height from the considered module is used. The exponential $\mathrm{e}^{a-\tilde{b}r}$ is then fitted a second time with the slope $\tilde{b}$ to infer the offset a.

However, the offset a is obviously not independent of the slope b (or $\tilde{b}$). In terms of error theory, the variables have to be transformed so that the off-diagonal elements of the covariant matrix become zero. This transformation is done by calculating the offset a_i of optical module i relative to the median offset $\tilde{a}_k$ of all optical modules k which have a similar slope $\tilde{b}_k$. This results in the relative sensitivity S_{rel} of the optical module. More precisely,

$$\begin{aligned} S_{\text{rel}} &= \mathrm{e}^{(a_i - \tilde{a}_i)/\tilde{a}_i} \\ \text{where} \quad \tilde{a}_i &= \text{median}\left\{ a_k \;\middle|\; |\tilde{b}_i - \tilde{b}_k| < 0.01\tilde{b}_i \right\}. \end{aligned} \qquad (9.11)$$

Course of Action

So the method works as follows: First one determines the track sensitivity S_{track}. With equation 9.6 the expectation value $\lambda(r > 0)$ is calculated. For all optical modules one fits the exponential e^{a-br} to $\lambda(r)$ at far distances to allow for scattering. To reduce the errors on the slope, one averages b as described and fits again, forcing this average slope. Thus one obtains the offset a. With equation 9.11 this yields the desired relative sensitivity S_{rel} of each optical module.

9.2 Defining the Event Sample

In order to determine S_{track}, one needs a sample of reconstructed events. The clean procedure would be to perform this reconstruction without the module that one wants to determine the sensitivity for. However, this path is very stony and takes up a lot of computational time. Instead, the standard reconstruction will be used here. This is justified because the error introduced is small: In the reconstruction of an event all optical modules which get a hit (number of channels `Nch`) are involved. The error introduced by one optical module is small if Nch $\gg 1$ which is basically always true: Already the standard trigger condition requires Nch ≥ 24, and the mean value is $\langle \text{Nch} \rangle \approx 40$.

To calculate the track sensitivity, we need a sample of events which satisfies the following three requirements as well as possible:

- The error Δr on the reconstructed distance should be as small as possible, so that $\lambda(r)$ can be measured accurately.
- The muon induced tracks should be as similar to each other as possible so that it can be excluded that optical modules at different positions within the detector are treated differently. In addition, the light emission along the track should be as smooth as possible. Minimaly ionizing muons will lead to tracks that fulfill this requirement.
- The sample should be as large as possible to restrain statistical errors.

Obviously, an optimization procedure is needed to find a good balance between the number of events on the one hand and their quality on the other hand. This procedure investigated on a sample of simulated minimum bias event, allowing for the analysis to be done in a blind way. The cuts are inferred by looking at various plots from simulated distributions. The actual values of the cuts are somewhat arbitrary, but one has to settle with something. The following sections try to motivate the chosen values as well as possible.

9.2.1 Zenith Cut

A cut on the reconstructed zenith angle is in order, because roughly horizontal events generally have bad quality. One reason was explained in the last chapter, another reason is the small lever arm for the reconstruction of horizontal events. Therefore I keep only events with zenith(Pandel) $< 60°$.

9.2.2 $\mathrm{d}E/\mathrm{d}x$ Cut

For this analysis only minimaly ionizing events which do not show too much statistical (variable) energy loss shall be selected. A measurement of the energy deposition $\mathrm{d}E/\mathrm{d}x$ is the number of hits `Nhit` over the length of the track in the detector. As an approximation of the latter I choose the length of direct hits with a time residual between -15 and 75 ns, projected on the

track of the Pandel fit (known as `LDirC`). A histogram of `Nhit/LDirC` is shown in figure 9.2. From the Bethe-Bloch formula we would expect this curve to fit to a Landau function, and indeed this is the case. As described in the figure caption I keep only events which have `Nhit/LDirC`(Pandel)$<$ 0.23 hits/m.

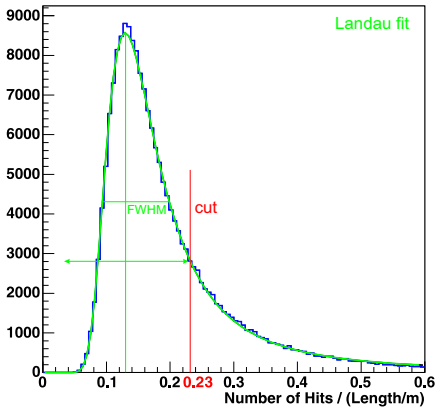

Figure 9.2: A beautiful surprise is the Landau fit to the reconstructed $\mathrm{d}E/\mathrm{d}x$ approximation. From the fit one gets the full width at half maximum as 0.1 hits/m. I cut away events which deposit more energy per length than this value added to the value at the peak. This is, as indicated in the figure, at 0.23 hits/m.

9.2.3 Smoothness Cut

Now that we have mainly events with a not too-high energy yield, this energy should be evenly distributed throughout the track. A measure for this is the smoothness parameter, which I cut to be $10^{-5} < |\text{smoothness}| < 0.3$, see figure 9.3. The lower bound is necessary because tracks that could not be fitted have their smoothness set to 0. The higher cut is just some value that seems appropriate when looking at various plots.

9.2.4 Cut to Make the Distance Error Small

Eventually the track sensitivity is needed as a function of the distance of the track to each given optical module. So this distance needs to be known accurately. It turns out that the paraboloid fit results in a good handle on the distance error. In figure 9.4 I plot what is called the resolution from the paraboloid fit (as explained in section 5.2.7. As motivated in the figure caption I cut on this parameter to be smaller than 3.3°.

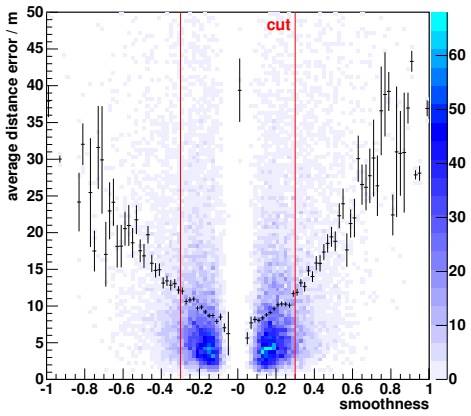

Figure 9.3: An example for one of the dependencies that were investigated to define the smoothness cut: Smoothness versus average distance error (Pandel track minus true track). In black, the mean of the respective smoothness bin is superimposed. It is difficult to argue for one or another value for a cut. Here, I am honest and do not argue at all, simply requiring $10^{-5} < |\text{smoothness}| < 0.3$.

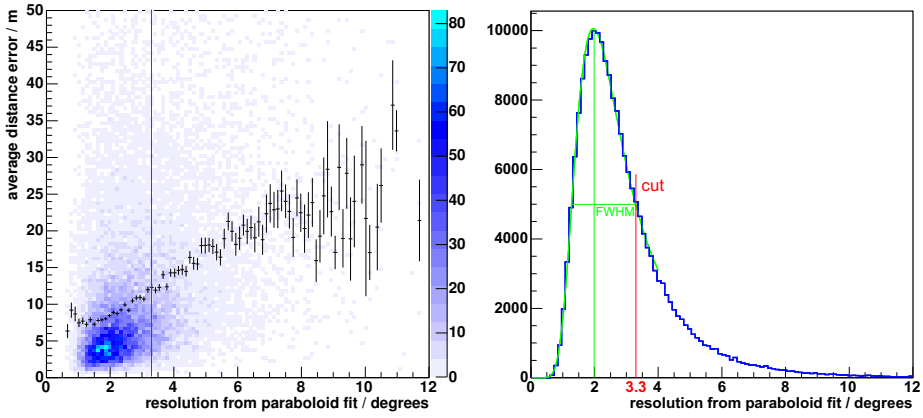

Figure 9.4: The resolution of the paraboloid fit in degrees. Left: As can be seen in this plot, this parameter gives a good handle on the average error on the distance of a track to each participating optical module: The better the resolution, the smaller the distance error. Right: I cut at a resolution $< 3.3°$ as constructed from this figure.

9.2.5 Cut on the Cherenkov Light Angle

As can be seen from figure 9.1 on page 73, vertically down-going events do not allow for unscattered Cherenkov photons to reach the photomultiplier tube, because the AMANDA modules are downward looking. Generally speaking, one would like to have horizontal Cherenkov photons with high statistics, but this is in contradiction to the zenith cut. As a compromise, another cut is applied, requesting the angle that the Cherenkov photons hitting the optical module make with the horizontal plane (ζ in figure 9.1) to be smaller than 15°. This angle is calculated for each event and each optical module, so whether an event survives this cut depends on the optical module considered.

9.2.6 Result of the Cuts

The application of the cuts improves the quality of the sample, as can be seen from figures 9.5 and 9.6. The error on the reconstructed distance is greatly reduced. The requirement Nch $\gg 1$ is satisfied even better. Also, one can now be confident that the event sample treats the individual optical modules equally.

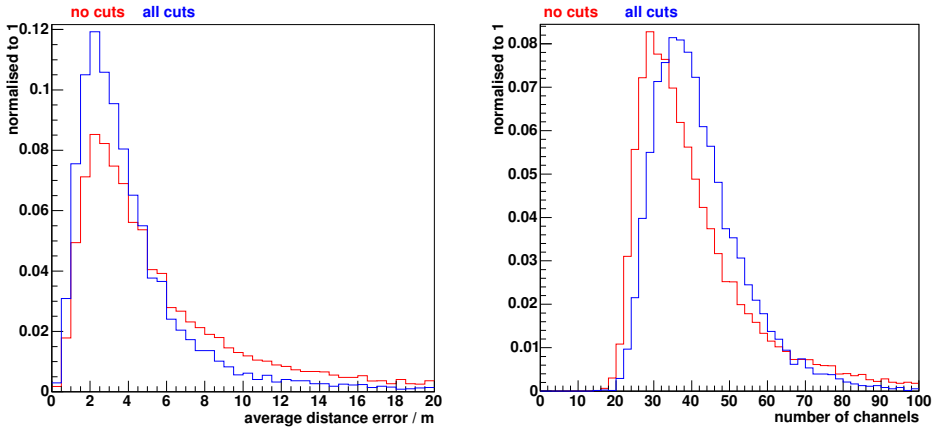

Figure 9.5: Left: The average error on the distance between the Pandel-reconstructed track and all optical modules that contribute to the event, before and after all the above mentioned cuts. The average 1σ error bar on the distance determination can easily be deduced from this plot and is cut down from 7 m to only 4 m. Right: The requirement Nch $\gg 1$ is well satisfied.

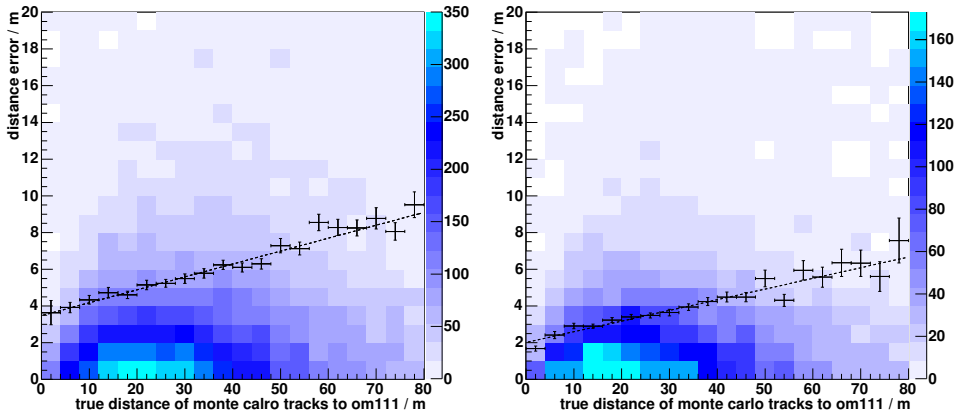

Figure 9.6: The impact of the quality cuts on the distance error (Pandel reconstructed minus true track), considering optical module number 111 as an example. Left: Without any cuts the mean of the distance error fits $\Delta d = 3.47\,\mathrm{m} + 0.07 r/\,\mathrm{m}$. Right: After the cuts, the mean becomes better by almost a factor of two and fits $\Delta d = 2.02\,\mathrm{m} + 0.06 r/\,\mathrm{m}$.

9.3 Monte Carlo Test

A large `PTD/mamint` Monte Carlo sample is used to test the method. As the relative sensitivities of the optical modules are previously not known, they are all set to 1.00 in the standard AMANDA simulation setup. The only exception are modules 1–86 which have their sensitivity set to 0.85 because these modules were the first to be deployed (strings 1–4) and are made from another glass. This glass is less transparent for ultra-violet light, so the modules are less sensitive. The idea is to recover these values from the simulation using the method described above. From the 680 optical modules, those are excluded that are *up-looking*, marked as *dead*, extremely *noisy* or have undetermined calibration constants. 477 optical modules remain for the test. This procedure qualifies as *blind analysis*, i.e. without optimizing the method on data.

As a typical example, the track sensitivity S_{track} and the expectation value $\lambda(r)$ of optical module number 111 as inferred from the simulation are plotted in figure 9.7. In distance, the values are binned in 4 m bins, which is consistent with the distance error as seen in the previous section. Between 20 m and 36 m an exponential $\lambda(r) = \mathrm{e}^{a-br}$ is fitted.

Once the fits are obtained for all optical modules, a second iteration fit is performed to reduce possible fluctuations. For this second fit, the slope b of the exponential is fixed to the median value $\tilde{b}$ of all optical modules that lie at most 10 m above or below the considered module (*running median*). Then the offset a is fitted again to the measured values, fixing $\tilde{b}$.

As slope and offset are not independent variables, the transformation as explained in section 9.1.4 is performed. Figures 9.8 and 9.9 show the

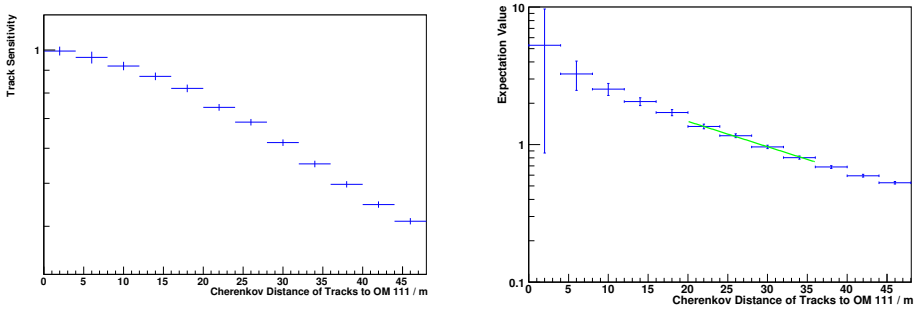

Figure 9.7: Track sensitivity $S_{\text{track}}(r)$ (left) and expectation value $\lambda(r)$ (right) for optical module 111 as a typical example. The track sensitivity saturates for small distances, but the expectation value does not. Because scattering is needed, the errors on $\lambda(r)$ become large for small r. Therefore the green exponential is fitted and extrapolated to $r = 0$ to find $\lambda(r = 0)$. To get reliable results one has to follow the transformation method as described in the text.

result for all optical modules as a function of their depth z. The slope $\tilde{b}$ indeed reflects the ice properties (superimposed in diagram 9.8) very well but deviates at lower depths. However, with the transformation of a, the strong dependency of S_{rel} on the depth z has gone.

For all 477 optical modules, figure 9.10 shows the relative sensitivities S_{rel}. For optical modules 87–680 the mean value $\langle S_{\text{rel}} \rangle$ should be unity (the way the modules are simulated) and is found to be 1.002. A Gaussian is fitted and leads to a standard deviation of $\sigma = 0.082 \pm 0.004$. In other words, with the method presented here it is possible to determine the relative sensitivities of the optical modules to $\pm 8\%$!

As the optical modules on strings 1–4 have their relative sensitivity simulated as 0.85, this allows for a second test. The light blue entries in figure 9.10 show the values for these modules, and indeed, the mean value is 0.88, compatible within less than one standard deviation with the expectation.

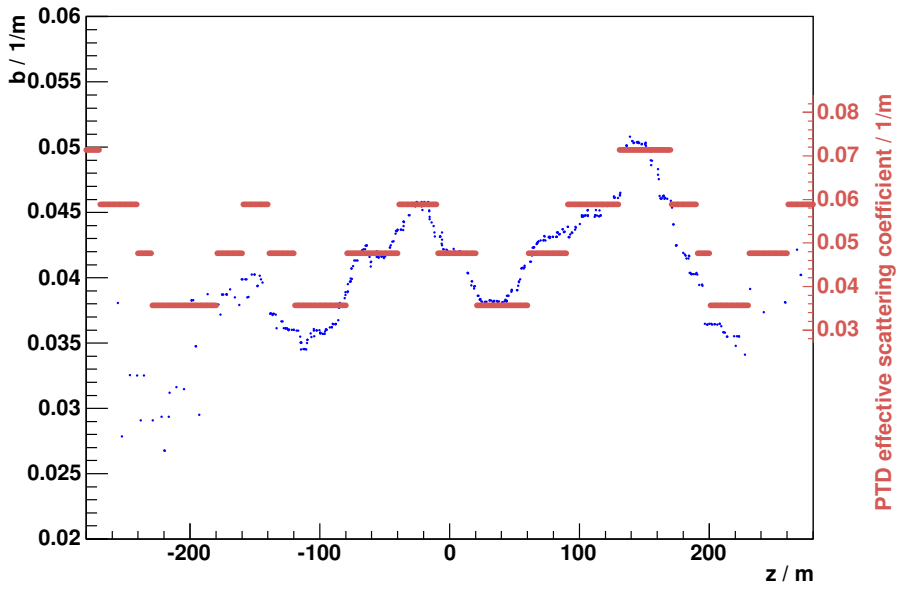

Figure 9.8: The slope $\tilde{b}$ of the exponential fit $\lambda(r) = e^{a-\tilde{b}r}$ versus depth follows the varying ice parameters. The blue values are the ones derived from analysis of the PTD simulation as described, the red values are the effective scattering coefficient intrinsic to the PTD tables.

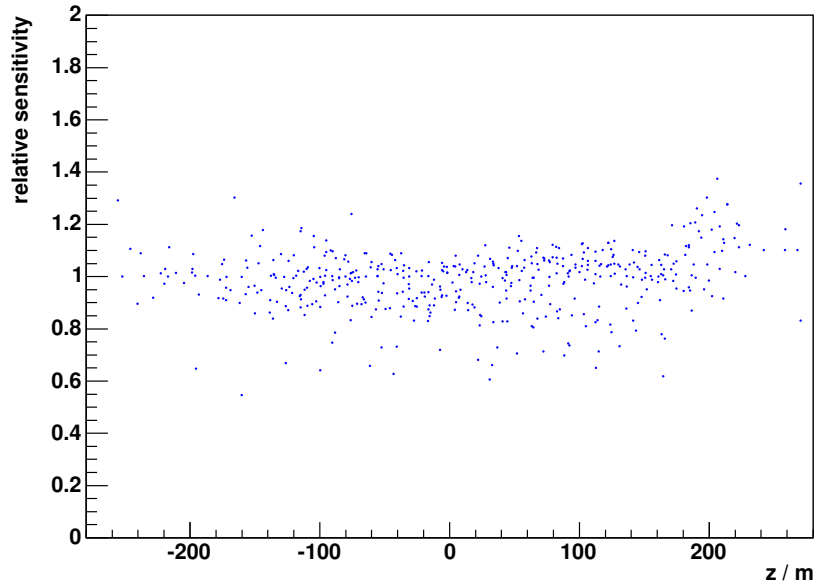

Figure 9.9: After the transformation of the offset a as explained in the text, the relative sensitivity S_{rel} is independent of the depth z.

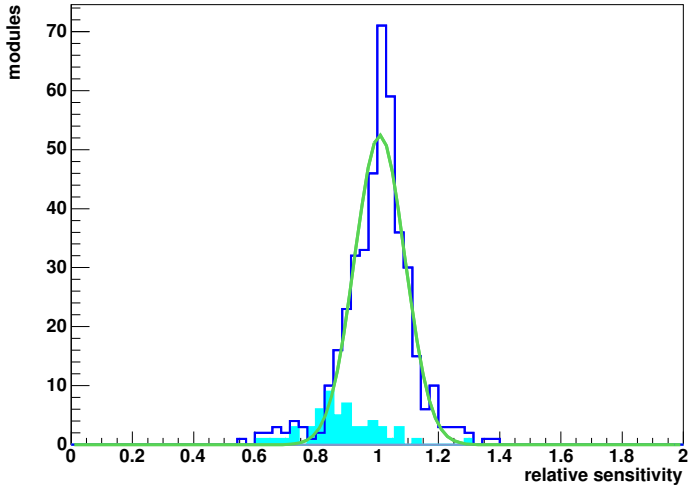

Figure 9.10: The accuracy of the analysis: In blue a histogram of the relative sensitivities S_{rel}. In green a Gaussian is fitted to estimate the error of the method. The method works to an accuracy of 8%. In light blue the values of optical modules 1–86 on the inner four strings.

9.4 Results From Data

The analyzed data set is a sample from 2001 with $\approx 10^7$ minimum bias events. Figure 9.11 shows the slope $\tilde{b}$ versus depth z. The structure shows many details, even more than the ice model that is used for the simulation with `Photonics`. Figure 9.12 shows the relative sensitivities S_{rel} versus depth; no dependence is seen.

In figure 9.13 the relative sensitivities are plotted in a histogram. The distribution is centered around $\langle S_{\mathrm{rel}} \rangle = 1.01$ with a spread of $\sigma_{\mathrm{Data}} = 0.14 \pm 0.01$. As the method has an intrinsic error of $\sigma_{\mathrm{MC}} = 0.082 \pm 0.004$, this translates into a spread of the optical modules' sensitivities of $\sigma = \sqrt{\sigma^2_{\mathrm{Data}} - \sigma^2_{\mathrm{MC}}} = 0.11 \pm 0.01$. Considering that previously a much larger spread was expected due to variations of optical gel parameters, this is not much.

Figure 9.13 also shows two surprises. The optical modules on strings 1–4 have an average sensitivity of only 0.727, thus are much less sensitive than previously thought. Implications of this finding to the understanding of the $\mathrm{CoG_z}$-events are topic of the next chapter. Another surprise comes from the optical modules on strings 11–13 which have an average sensitivity of 1.206. They are therefore *more* sensitive than the average. Strings 11–13 have been deployed in the 1998/1999 season, but performed below expectation. Therefore, their high voltage was increased. This may be the reason that today these modules yield more hits than average. Figure 9.14 shows the average relative sensitivity of all strings.

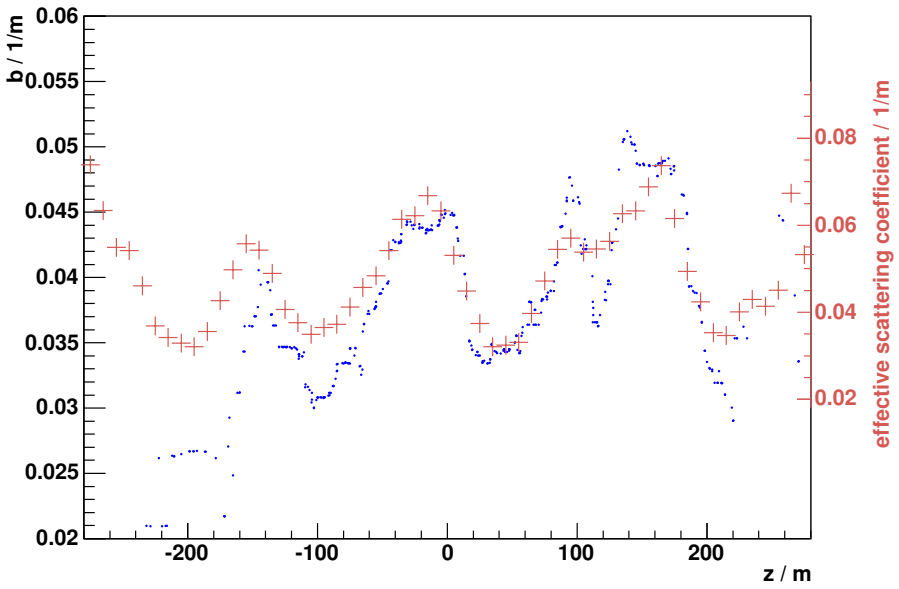

Figure 9.11: The slope $\tilde{b}$ of the exponential fit $\lambda(r) = \mathrm{e}^{a-\tilde{b}r}$ versus depth (shown in blue) shows the varying ice parameters with great detail. This result shows more structure than the ice model underlying `Photonics` (superimposed in red).

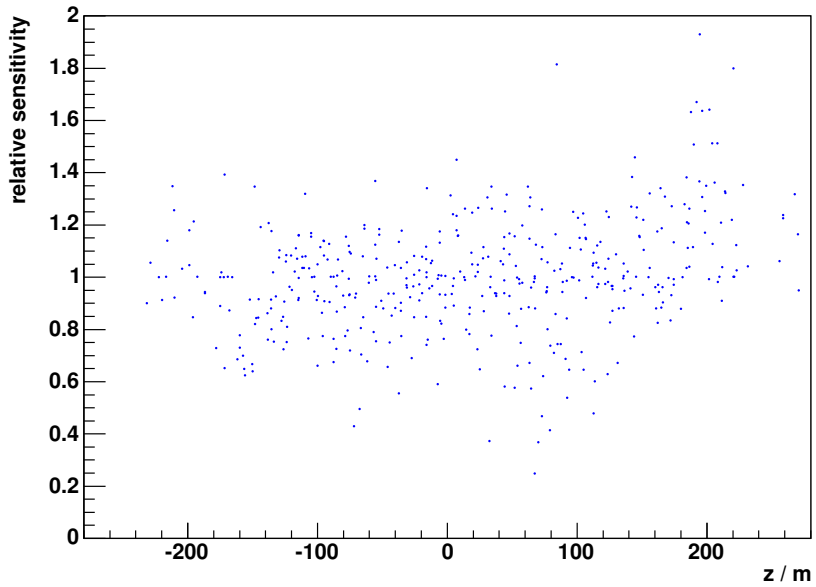

Figure 9.12: The relative sensitivities S_{rel} as inferred from the 2001 data sample are independent of z.

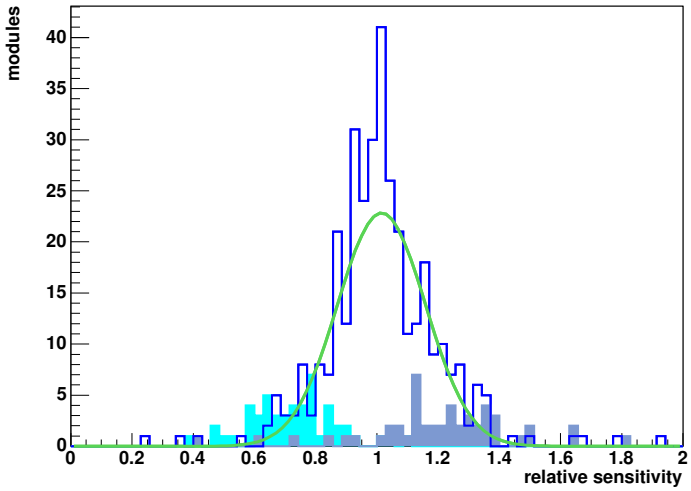

Figure 9.13: The relative sensitivities S_{rel} of the optical modules as of 2001. As in the case of the test against the simulation, a Gaussian (in green) is fitted to the histogram (in blue). As the width of this Gaussian ($\sigma = 0.14 \pm 0.01$) is larger than the one from simulation, the optical modules have a measurable spread of sensitivities. In light blue, the relative sensitivities of optical modules on strings 1–4 are plotted, showing that they are less sensitive than previously thought. In darker blue the optical modules of strings 11–13 are plotted, showing that these have a sensitivity higher than average.

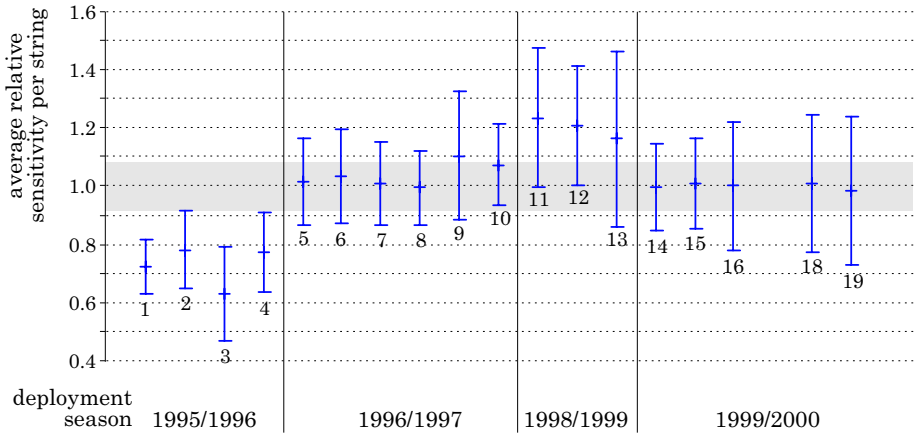

Figure 9.14: Here the average sensitivity of the optical modules on each string are plotted together with the standard deviation. Clearly, modules on strings 1–4 are less sensitive, whereas modules on strings 11–13 are more sensitive than average. Also, the years of deployment are shown. There is no indication of an ageing effect. String 17 is missing as it got stuck during deployment and is excluded from data analysis.

9.5 Conclusion

A method was introduced to infer the relative sensitivities of optical modules from down-going muon data. A test against a Monte Carlo sample was successful and yielded an estimate for the method to be accurate to $\pm 8\%$. The analysis was carried out on 2001 data, and the relative sensitivities of the AMANDA optical modules were determined. In doing so, optical modules on strings 1–4 were found to be much less sensitive than expected, while these on strings 11–13 were found to yield more hits. This allows to significantly reduce the systematic error of AMANDA analyses such as the search for point sources. In addition, the ice parameters were determined with good precision, which allows for cross-checks with other measurements.

Chapter 10

The Hollow-Bean-Conjecture

Intent: So far, chapter 8 about `Photonics` and chapter 9 about the sensitivities seem to be somewhat unrelated, except that they both address sources of systematic errors. But while working on them, it turned out that they could be closely related by the CoG_z-events. The connection is summarized in the *Hollow-Bean-Conjecture*, which may be a big step forward in the understanding of the AMANDA signal region below horizon.

Organization: In section 10.1, data is compared with the simulation using `PTD` on both minimum bias level and for up-going events. A possible explanation for the observed discrepancy is given in section 10.2. Results from a first specialized simulation support this explanation as illustrated in section 10.3.

10.1 CoG_x-CoG_y-Distributions

The most important signal region for AMANDA is the region below horizon. It has been shown that in this region the expected signal from atmospheric and extraterrestrial neutrinos is outnumbered by mis-reconstructed down-going muons by a factor of 1000. These mis-reconstructed events show a distinctive layered structure of their centers of gravity (CoG_z) following varying ice properties. The precise modeling of the ice parameters with `Photonics` was believed to be able to explain these events. However, the agreement (figure 8.5 on page 68) with data is disappointing. First simulations with the bug-free version of `Photonics` show no significant improvement in the understanding of CoG_z-events [6]. So the ice properties alone can not be responsible for the mis-reconstruction of events.

Instead of just plotting the z-coordinate of the center of gravity (CoG_z), figure 10.1 plots the center of gravity in the x-y-plane as a two-dimensional histogram for minimum bias data. The figure may well be described as that of a *bean*. As the AMANDA detector is a very inhomogeneous device, the strong asymmetry of the figure is no big surprise. The figure also shows the histogram for events from a standard simulation using `dCorsika` and `PTD`. As has been noted before, the simulation agrees very well with data on this minimum bias level.

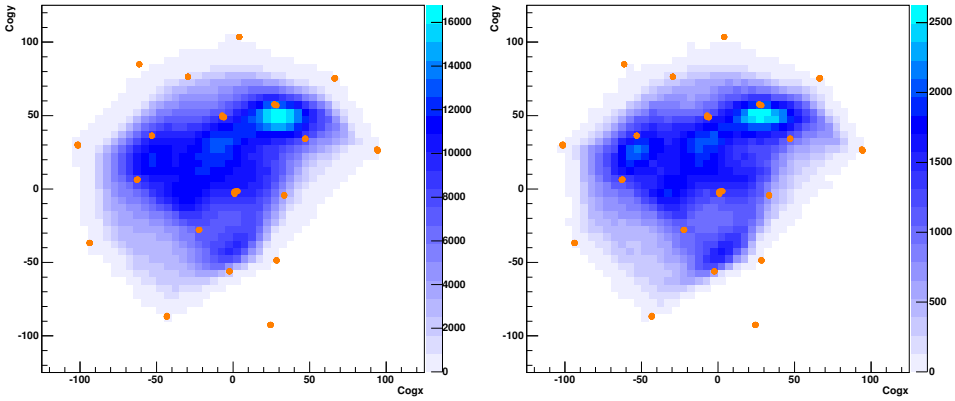

Figure 10.1: Looking at the detector from above, the distributions of the centers of gravity of minimum bias events are plotted. Left: minimum bias data. Right: minimum bias simulation using PTD. The distributions match well. In Orange the positions of the strings; for the string numbers compare with figure 4.6 on page 33.

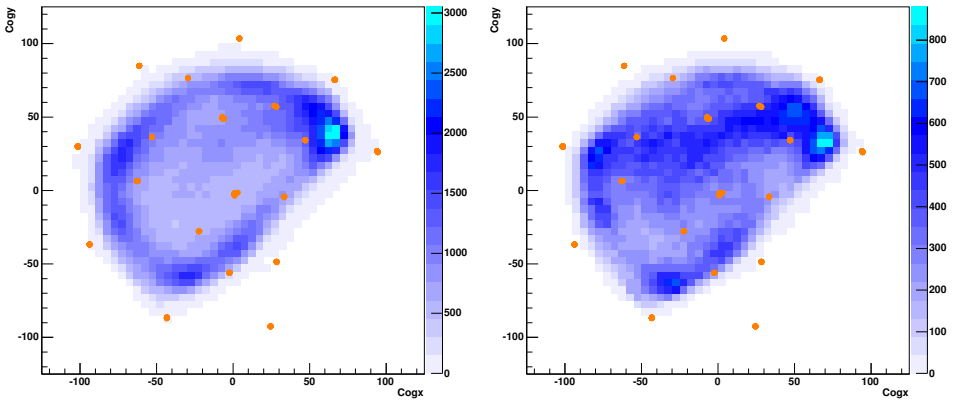

Figure 10.2: The centers of gravity in the x-y-plane, i.e. looking at the detector from above. Left: For up-going muon data, the CoG_z-events form a clear ring-like structure. Right: The PTD simulation fails to reproduce this pattern. Instead, in addition to the events on the ring, parts of the center are also filled.

But the situation changes once more when only events from below horizon are plotted. Figure 10.2 shows the distribution of the centers of gravity in the x-y-plane. A distinctive ringlike structure (like a *hollow bean*) emerges, whereas the distribution from the `PTD` simulation looks very different. There, the ringlike structure is also visible, but the bean is not hollow, and many entries occur at the center of the detector. Thus, once more, the standard `PTD` simulation is not capable of reproducing the CoG_z events with adequate accuracy.

Unfortunately, it is not easy to produce these two-dimensional plots, which is why this effect has not been noted before. From 1000 generated down-going muons only one is mis-reconstructed as up-going. Thus for these plots, very large simulations are needed.

10.2 The Conjecture

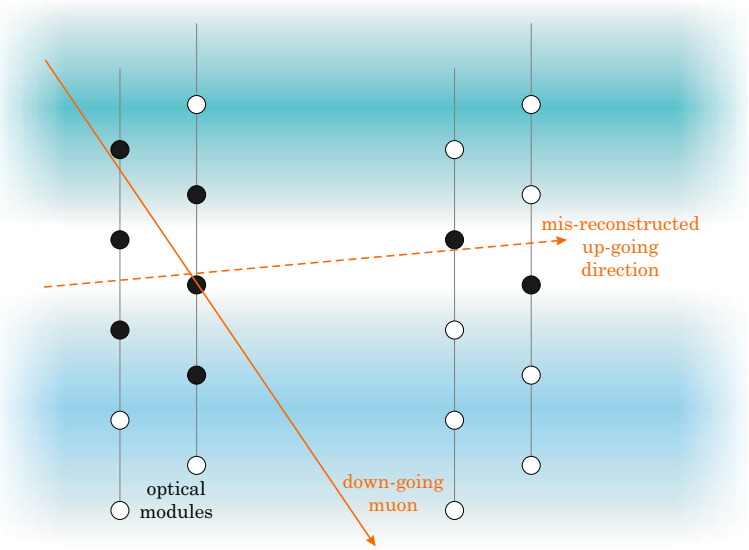

Figure 10.3: To motivate the hollow-bean-conjecture, the sensitivity of the detector is exaggerated as that of a ring-like structure. Then, light from a down-going muon may reach the other side of the ring only through more transparent layers of ice. This may lead to mis-reconstructed events as shown. In this case, the z-coordinate of the center of gravity of these events would peak in coincidence with layers of highly transparent ice.

As the simulation could not be repeated with `Photonics`, the following line of argument only qualifies as a conjecture. The idea is the following: In the simulation using `PTD`, many mis-reconstructed events have their center of gravity close to the center of the detector. But as has been shown in the previous chapter, the simulation over-estimates the sensitivity of the optical modules in this region by 17%. Were the sensitivity simulated cor-

rectly, these events centering in the middle might not be able trigger the detector. Therefore, an improved modeling of the detector using the correct sensitivities may have a significant contribution to the CoG_z-structure and to the correct modeling of AMANDA's signal region. This is what I call the *hollow-bean-conjecture.*

This point of view is motivated by the following argument: For the sake of simplicity, imagine the more extreme case in which the detector is a ring-like device where the optical modules of the inner strings are not sensitive to light at all. Suppose a down-going muon with low energy as depicted in figure 10.3 hits the detector. Light will be more likely to reach the other side of the ring if it propagates through layers of highly transparent ice. In this case, some hits would also occur on the right side in figure 10.3. If the light output is strong enough to trigger the detector, then the reconstruction algorithms are likely to mis-reconstruct this event. In this case, the center of gravity of the event would coincide with the transparent ice layer. Thus the *hollow bean conjecture* explains an additional contribution to the CoG_z-structure.

10.3 Supporting the Conjecture

Once again, to prove the conjecture, a simulation with `Photonics` would be necessary. But the nearing deadline for the thesis required a different approach which at least supports the conjecture. For this, a large existing sample of `dCorsika` events that were simulated with `PTD/mamint` is used. The simulation is modified by marking all optical modules on strings 1–4 as dead. The events are then re-triggering and reconstructed using the standard procedure. This is an exaggeration of the result of the previous chapter, namely, that the optical modules on these inner four strings are less sensitive to light than previously thought. With this reconstruction, figure 10.4 is produced, comparing this ad hoc simulation with both the standard `PTD` simulation and data. Clearly, changing the sensitivities to this extreme values has a strong effect on the CoG_z structure and therewith on the mis-reconstruction of events.

10.4 Conclusion

It was shown that for the correct simulation of the AMANDA signal region, the proper simulation of module sensitivities can have a strong influence. In particular, the hollow-bean-conjecture holds that a correct simulation of the inner four strings is the key to a major contribution to the CoG_z structure. In this case, the simulation of varying ice properties alone could never be able to fully reproduce the observed CoG_z structure.

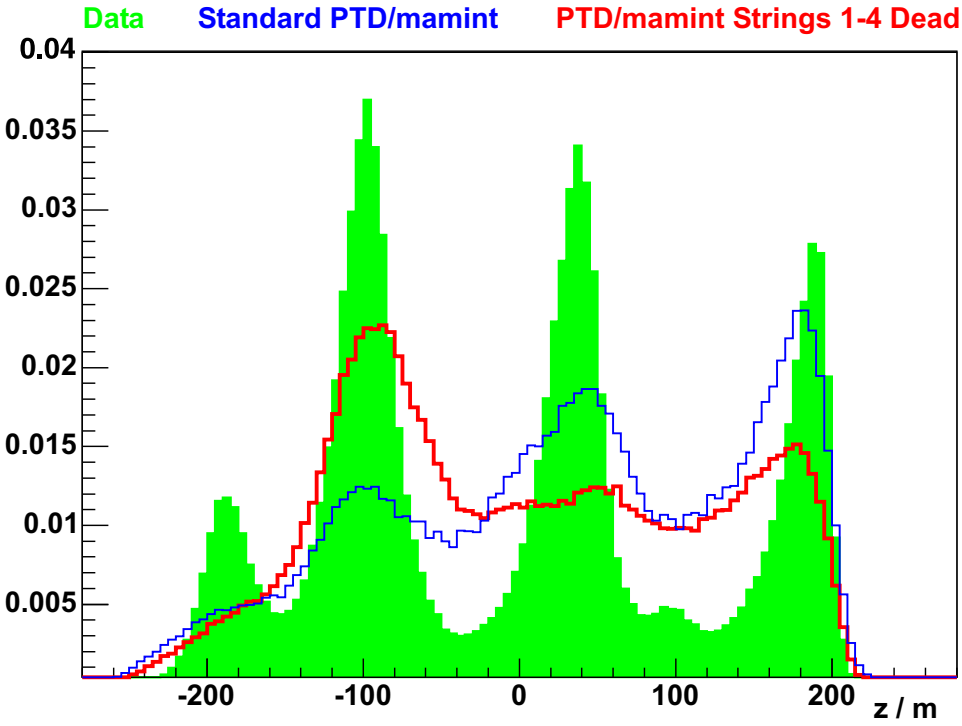

Figure 10.4: A comparison of 2001 data events with the standard PTD simulation and the ad hoc PTD simulation as described in the text. Plotted are the z-coordinates of the Centers of Gravity of events below the horizon (level 3). In green, the data shows the distinctive layered structure. The corresponding distribution from the standard PTD simulation is shown in blue. In red, the histogram from the ad hoc simulation where the inner four strings are marked as dead. Clearly there is a strong influence of the detector topology (and thus of the sensitivities) on the mis-reconstruction of events: the CoG_z-structure changes its shape dramatically between the two simulations.

Chapter 11

Outlook

AMANDA data is still streaming in. The detector will continue operation as a low-energy sub-detector of the much larger IceCube detector. This allows important cross-checks of the performance of the new detector. If not even AMANDA, at least the cubic-kilometer-sized IceCube will soon detect the first high energy neutrino point sources. Many other exiting discoveries lie ahead.

Point Source Searches

The time integrated search for high energy neutrino point sources has not yet succeeded. With the present technology, the search for time variable sources is very promising. To do so, one analyzes angular and temporal correlations not only within an experiment, but also between different experiments (e.g. [99]). Multi-messenger studies (e.g. [2, 41]) will be a focus of future AMANDA research. Also, flary astrophysical events (like the one described by the INTEGRAL collaboration [52]) are promising candidates for first detected neutrino sources as the short timescales allow strong suppression of background.

`Photonics`

The `Photonics` software is now available in a stable and seemingly bug-free version. This allows to repeat the simulation presented here. It is then possible to compare `Photonics` to the previous modeling which will increase the confidence in the performance of `Photonics`. This is particularly important for reconstruction of the first incoming IceCube events.

Sensitivities

The knowledge of the actual sensitivities can easily be incorporated into the detector simulation. This will improve the agreement of the simulation with the data. One can extend the sensitivity analysis to other parameter dependencies like the incident zenith angle of the Cherenkov photon on the optical module to make the simulation even more accurate. The method

is trivially scalable to the much larger IceCube detector and will be an important method to determine and cross check the sensitivities there. The error on the reconstructed distance of tracks to optical modules is very small ($\approx 2\,\mathrm{m}$) for tracks that pass close to the module. This should allow at least a rough determination of the hole ice properties.

Hollow-Bean-Conjecture

The next step concerning this matter is to do a large simulation with `Photonics` together with the accurate modeling of the optical modules' sensitivities. The important plot to look at is the distribution of the centers of gravity of events from below horizon. It will be very interesting to see whether the data features can be fully reproduced or whether other improvements on the simulation have to be made. With the understanding of the $\mathrm{CoG_z}$ events it will also be possible to think of an algorithm that reliably excludes these events from point source searches. The improved understanding will result in lower systematical uncertainties and thus in better limits, or even allow to tighten the quality cuts leading to a discovery of a neutrino point source.

Acknowledgments

This work would not have been possible without the help of many people, so acknowledgments are in order. I am thankful to Prof. Dr. Steiner and Prof. Dr. Jex who spontaneously agreed to referee my thesis, and the members of the Prüfungsausschuß who permitted this external work at DESY Zeuthen. I am very grateful to Christian Spiering for his warm welcome to the neutrino group. Working in the Zeuthen group is great fun and something I really enjoyed. Thanks go to Stefan who makes a great group leader, to Mike (good luck with the Cosmic Ray Trigger), to Rolf and Ralf, and of course to Hermann. I am very grateful to Elisa, David, Tonio, Henrike, Stefan, Bernhard, Sebastian, Oxana, Helge and Jan. Not last and not least I am indebted to Markus without whom this thesis would lack ideas and progress. Special thanks go to Christian, Elisa, Markus, Bernhard and Ciaran for proofreading. The infrastructure at DESY Zeuthen is just phenomenal and I am very grateful to the people that keep it going, as there are Stephan, Andreas and Simone, Katrin, Ms Baer and Ms Langner, Martina, Ulrike, Axel, Christine, Susann and Heidi, Evelin and Carola, Mr. Zieger, Mr. Schilling and Mr. Tschesch, and a special thank you to Mr. Zimmermann and his team. Of the many collaboration members I was allowed to meet or work with I am particularly grateful to Tom, Kurt, Christopher, Jessica, and Johan for a very good teamwork, and, in a very special sense, to Stephan without whom I had never investigated the sensitivities. Now, obviously I couldn't have put this work together without my parents Margot and Heinz who always are a great support, so thank you very much for your reliable comfort and hearty encouragement. Many thanks go to Heike and Axel, and a big thank you for a lot of quite important support to Franziska. This work is heavily supported by Calvin and Hobbes. Special thanks go to Uli and Thomas and to all members of the Volkssternwarte Laupheim e.V. Also I thank Mr Kauer and Ms Lebek. For two images in this thesis I am especially grateful: To Michael Bischof for the rendering of the Earth image in figure 4.7, and special thanks go to Tom Gaisser as he gave me figure 2.1 for my thesis even before he published it himself, which he will do in the new edition of his excellent book that will appear soon [36]. In case I have forgotten somebody, don't worry, I am grateful to you, too. And finally, a big applause to the reader of all this – I hope you enjoyed reading as much as I enjoyed writing; I really did.

Erklärung

Hiermit erkläre ich, dass ich die vorliegende Arbeit selbst verfasst habe und keine anderen als die angegebenen Quellen und Hilfsmittel benutzt habe.

Rafael Lang, Zeuthen, September 2005

Bibliography

[1] M. Ackermann et al. (the AMANDA collaboration), *Investigation of Seasonal Variations in the Atmospheric Neutrino Rate with the AMANDA-II Neutrino Telescope*, in: Proceedings of the 29th International Cosmic Ray Conference, Pune, India (2005), e-print `arXiv:astro-ph/astro-ph/0509330`.

[2] M. Ackermann et al. (the AMANDA collaboration), *Multi-Wavelenght Comparison of Selected Neutrino Point Source Candidates*, in: Proceedings of the 29th International Cosmic Ray Conference, Pune, India (2005), e-print `arXiv:astro-ph/astro-ph/0509330`.

[3] M. Ackermann et al. (the AMANDA collaboration), *Search for High-Energy Neutrino Point Sources in the Northern Hemisphere with the AMANDA-II Neutrino Telescope*, in: Proceedings of the 29th International Cosmic Ray Conference, Pune, India (2005), e-print `arXiv:astro-ph/astro-ph/0509330`.

[4] M. Ackermann et al. (the AMANDA collaboration), *Three-year search for extraterrestrial point sources of neutrinos with AMANDA-II*, (2005), to be published.

[5] M. Ackermann and M. Leuthold, *The AMANDA Datahandler*, web site. URL `http://www-zeuthen.desy.de/nuastro/protected/datahandler.html`, 2003.

[6] M. Ackermann, private communication.

[7] J. A. Aguilar et al. (the ANTARES collaboration), *Transmission of light in deep sea water at the site of the Antares neutrino telescope*, Astroparticle Physics **23** (2005), 131–155, e-print `arXiv:astro-ph/0412126`.

[8] F. A. Aharonian et al. (the H.E.S.S. collaboration), *High-energy particle acceleration in the shell of a supernova remnant*, Nature **432** (2004), 75–77, e-print `arXiv:astro-ph/0411533`.

[9] F. A. Aharonian et al. (the H.E.S.S. collaboration), *A New Population of Very High Energy Gamma-Ray Sources in the Milky Way*, Science **307** (2005), 1938–1942, e-print `arXiv:astro-ph/0504380`.

[10] J. Ahrens et al. (the AMANDA collaboration), *Observation of High Energy Atmospheric Neutrinos with the Antarctic Muon and Neutrino Detector Array*, Physical Review D **66** (2002), e-print `arXiv:astro-ph/0205109`.

[11] J. Ahrens at al. (the AMANDA collaboration), *Measurement of the cosmic ray composition at the knee with the SPASE-2/AMANDA-B10 detectors*, Astroparticle Physics **21** (2004), 565–581.

[12] J. Ahrens at al. (the AMANDA collaboration), *Muon track reconstruction and data selection techniques in AMANDA*, Nuclear Instruments and Methods in Physics Research A **524** (2004), 169–194.

[13] J. Ahrens at al. (the AMANDA collaboration), *Search for Extraterrestrial Point Sources of Neutrinos with AMANDA-II*, Physical Review Letters **92** (2004), no. 7, 071102.

[14] The Barwick Group for the AMANDA collaboration, *AMANDA-II project - official site*, web site. URL `http://amanda.uci.edu/`.

[15] E. Andres at al. (the AMANDA collaboration), *The AMANDA neutrino telescope: principle of operation and first results*, Astroparticle Physics **13** (2000), 1–20.

[16] Talks given at the first workshop on Acoustic and Radio EeV Neutrino detection Activities (ARENA) in Zeuthen, 2005, available from `http://www-zeuthen.desy.de/arena/`.

[17] H. Athar, M. Jezabek, and O. Yasuda, *Effects of neutrino mixing on high-energy cosmic neutrino flux*, Physical Review D **62** (2000), 103007, e-print `arXiv:hep-ph/0005104`.

[18] W. Bednarek and R. J. Protheroe, *Gamma Rays and Neutrinos from the Crab Nebula Produced by Pulsar Accelerated Nuclei*, Physical Review Letters **79** (1997), 2616–2619.

[19] E. Bernardini for the AMANDA collaboration, *New results from the AMANDA Neutrino Telescope*, Nuclear Physics B (Proceedings Supplements) **145** (2005), 319–322.

[20] A. P. v. C. Biron, *Search for Atmospheric Muon-Neutrinos and Extraterrestric Neutrino Point Sources in the 1997 AMANDA-B10 Data*, Ph.D. thesis, Humboldt-Universität zu Berlin, 2002.

[21] D. D. Blankenship and Instrument Definition Team for a Europa Radar Sounder, *Subsurface Evaluation of Europan Ice-Ocean Interchange Processes, Using an Orbiting Ice Penetrating Radar*, abstract 1854, XXXII Lunar and Planetary Conference, Houston (2001).

[22] S. Böser, *Separation of atmospheric neutrinos with the AMANDA-II detector*, Diplom thesis, Technische Universität München, 2002.

[23] M. Böttcher and C. D. Dermer, *An Evolutionary Scenario for Blazar Unification*, The Astrophysical Journal **564** (2002), 86–91, also available from `http://www.phy.ohiou.edu/~mboett/galaxyevolution.html`.

[24] N. E. Bramall et al. (the IceCube collaboration), *A deep high-resolution optical log of dust, ash, and stratigraphy in South Pole glacial ice*, Geophysical Research Letters, to be published (2005).

[25] D. E. A. Castillo, *Analysis of Angular Correlations from AMANDA Data 2000-2003*, DESY summer student report, available from `http://www-zeuthen.desy.de/students/2004/index.html`, 2004.

[26] D. Chirkin, *dCORSIKA - CORSIKA for AMANDA*, available from `http://amanda.berkeley.edu/~dima/work/CORSIKA/`.

[27] D. Chirkin, *Muon propagation code in Java*, available from `http://area51.berkeley.edu/~dima/work/MUONPR/`.

[28] D. Chirkin and W. Rhode, *Muon Monte Carlo: a new high-precision tool for muon propagation through matter*, e-print `arXiv:hep-ph/0407075`, 2004.

[29] *CORSIKA (COsmic Ray SImulations for KAscade)*, available from `http://amanda.wisc.edu/software/corsika/`.

[30] P. Desiati, *e-mail to datamc@amanda.wisc.edu on July 15th, 2003*, posted at `http://amanda.wisc.edu/simulation/simu2002_v001/NUSIM_Run_Numbers.txt`.

[31] P. Desiati, *SimuPerl v0.4 User Manual*, available from `http://amanda.wisc.edu/software/`, probably under `simuperl/` or under `simu2002_v001/simu2002_v001.shtml`.

[32] S. Eidelman et al., *Review of Particle Physics*, Physics Letters B **592** (2004), URL `http://pdg.lbl.gov`.

[33] EPICA community members, *Eight glacial cycles from an Antarctic ice core*, Nature **429** (2004), 623–628, (this Nature issue has a focus on Antarctic glacier with many interesting articles).

[34] T. Ericson and S. L. Glashow, *Six-Fermion Weak Interactions*, Physical Review **113** (1964), no. 1B, B130–B131.

[35] E. Fermi, *On the Origin of the Cosmic Radiation*, Physical Review **75** (1949), no. 8, 1169–1174.

[36] T. Gaisser, *Cosmic Rays and Particle Physics*, Cambridge University Press, Cambridge, 1990.

[37] T. Gaisser, *Outstanding Problems in Particle Astrophysics*, e-print `arXiv:astro-ph/0501195`, 2005.

[38] R. J. Gaitskell, *Direct Detection of Dark Matter*, Annual Review of Nuclear Particle Science **54** (2004), 315–359.

[39] A. Gazizov and M. Kowalski, *ANIS: High Energy Neutrino Generator for Neutrino Telescopes*, e-print `arXiv:astro-ph/0406439`, 2004.

[40] K. Greisen, *Cosmic Ray Showers*, Annual Reviews of Nuclear Science **271** (1960), 63–108.

[41] F. Halzen, *Multi-Messenger Astronomy: Cosmic Rays, Gamma-Rays and Neutrinos*, e-print `arXiv:astro-ph/0302489`, 2003.

[42] T. Hauschildt, *Search for Cosmic Point Sources of High Energy Neutrinos with the AMANDA-II Detector*, Ph.D. thesis, Humboldt-Universität zu Berlin, 2004.

[43] D. Heck, *CORSIKA: an Air Shower Simulation Program*, web site. URL: `http://www-ik.fzk.de/corsika/`, 2005.

[44] The H.E.S.S. collaboration, *The H.E.S.S. project, an Array of Imaging Atmospheric Cherenkov Telescopes*, web site. URL: `http://www.mpi-hd.mpg.de/hfm/HESS/`, 2005.

[45] V. F. Hess, *Über Beobachtungen der durchdringenden Strahlung bei sieben Freiballonfahrten*, Physikalische Zeitschrift **13** (1912), 1084–1091 (in German).

[46] G. Hill et al., *Evidence for insufficient absorption in the AMANDA Monte Carlo*, web site. URL: `http://amanda.wisc.edu/ghill/absorption/absorption.html`.

[47] D. Hooper and J. Silk, *Searching for dark matter with neutrino telescopes*, New Journal of Physics **6** (2004).

[48] J. R. Hörandel, *Models of the knee in the energy spectrum of cosmic rays*, Astroparticle Physics **21** (2004), 241–265.

[49] J. R. Hörandel, *Overview on direct and indirect measurements of cosmic rays*, e-print `arXiv:astro-ph/0501251`, 2005.

[50] S. Hundertmark, *Simulation und Analyse von Myonereignissen im AMANDA-B4-Neutrinoteleskop*, Ph.D. thesis, Humboldt-Universität zu Berlin, 1999.

[51] S. Hundertmark, *Scatserver, Interface to Photonics*, available from `http://www.physto.se/~amanda/local/amasim_and_co/scatserver/scatserver_%main.html`, 2005.

[52] K. Hurley et al., *An exceptionally bright flare from SGR 1806-20 and the origins of short-duration γ-ray bursts*, Nature **434** (2005), 1098–1103.

[53] G. Japaridze and M. Ribordy, *Realistic arrival time distribution from an isotropic light source*, e-print `arXiv:astro-ph/0506136`, 2005.

[54] L. Ju, D. G. Blair, and C. Zhao, *Detection of gravitational waves*, Reports on Progress in Physics **63** (2000), 1317–1427, available from `http://www.gravity.uwa.edu.au/DetGW/review.pdf`.

[55] A. Karle, *Monte Carlo simulation of photon transport and detection in deep ice: muons and cascades*, (1999), 174–185, in: Simulation and Analysis Methods for Large Neutrino Telescopes, ed. C. Spiering, DESY-PROC-1999-01.

[56] A. Karle, *PTD - Photon Transport and Detection*, web site. URL `http://www.amanda.wisc.edu/karle/ptd/`, 1999.

[57] H. Kolanoski, *Skript zur Vorlesung Struktur der Materie c*, in German, `http://www-zeuthen.desy.de/~kolanosk/struma0304/skript.html`, 2004.

[58] M. Kowalski, *Search for Neutrino-Induced Cascades with the AMANDA-II Detector*, Ph.D. thesis, Humboldt-Universität zu Berlin, 2004.

[59] M. Kowalski and A. Gazizov, *ANIS (All Neutrino Interaction Generator)*, available from `http://www.ifh.de/~mkowalsk/anis.html`.

[60] R. Lang, *Amasim and Photonics*, web page. URL `http://www-zeuthen.desy.de/~rlang/amanpho/`, 2004.

[61] R. Lang, *Angular and Temporal Correlations*, talk given at the AMANDA/IceCube Uppsala meeting, October 2004. available from `http://www-zeuthen.desy.de/~rlang/`, 2004.

[62] R. Lang and M. Ackermann, *Simuperl and Photonics*, talk given at the Amanda/IceCube Meeting, Berkley, March 2005. available from `http://www-zeuthen.desy.de/~rlang/`, 2005.

[63] R. Lang and M. Ackermann, *Tiefenabhängige Eisparameter im AMANDA Experiment*, talk given at the DPG Frühjahrstagung Berlin, March 2005, in German. available from `http://www-zeuthen.desy.de/~rlang/`, 2005.

[64] P. Langacker, J. Erler, and E. Peinado, *Neutrino Physics*, Lectures presented by Paul Langacker at the 11th Mexican School of Particles and Fields, Xalapa, Mexico (2004), e-print `arXiv:hep-ph/0506257`.

[65] P. Langacker, J. P. Leveille, and J. Sheiman, *On the detection of cosmological neutrinos by coherent scattering*, Physical Review D **27** (1983), no. 6, 1228–1242.

[66] J. G. Learned and K. Mannheim, *High-Energy Neutrino Astrophysics*, Annual Review of Nuclear and Particle Science **50** (2000), 679–749.

[67] W. R. Leo, *Techniques for Nuclear and Particle Physics Experiments — A How-to Approach*, Springer Verlag, Berlin, 1994.

[68] E. Lohrmann and D. Haidt, *Neutrino-Oszillationen*, Physik in unserer Zeit **2** (2000), 64–72 (in German).

[69] J. Lundberg, *Berkley talk Animations*, web site. URL: `http://www.physto.se/~johan/amanda/berkeley2005/index.html`, 2005.

[70] D. Malin, *Anglo-Australian Observatory Astronomical Images (50+ all-time favorites)*, web site. URL: `http://www.aao.gov.au/images/index.html`, 2004.

[71] M. A. Markov and I. M. Zheleznykh, High-energy Neutrino Physics D **577** (1960), Referenced in a talk given by Igor Zheleznykh at the ARENA Workshop, available from `http://www-zeuthen.desy.de/arena/talks/TuesdayI_Introduction_Theory/2-Z%eleznykh.ppt`. However, I was not able to root this paper up.

[72] J. C. R. Martino, *Detector analysis using atmospheric muons*, talk given at the AMANDA collaboration meeting in Stockholm, June 2002, available from `http://www.physto.se/~amanda/sthlm2002/`, 2002.

[73] J. C. R. Martino, *A Study of the AMANDA Detector Using Atmospheric Muons*, Ph.D. thesis, Stockholm University, 2003.

[74] S. L. Miller, *Clathrate Hydrates of Air in Antarctic ice*, Science **165** (1969), 489–490.

[75] P. Miocinović, *Muon energy reconstruction in the Antarctic Muon And Neutrino Detector Array (AMANDA)*, Ph.D. thesis, University of California at Berkeley, 2001.

[76] H. Motz and L. I. Schiff, *Cerenkov Radiation in a Dispersive Medium*, American Journal of Physics **21** (1953), 258–259.

[77] *Nusim*, available from `http://amanda.wisc.edu/software/nusim/`.

[78] R. Nahnhauer, private communication.

[79] NASA Space Telescope Science Institute, *Hubble Heritage Image Gallery*, web site. URL: `http://heritage.stsci.edu/gallery/gallery.html`.

[80] T. Neunhöffer, *Estimating the angular resolution of tracks in neutrino telescopes based on a likelihood analysis*, e-print `arXiv:astro-ph/0403367`, submitted to Astroparticle Physics, 2004.

[81] Space Telescope Science Institute's Office of Public Outreach, *Hubblesite: NASA's Hubble Space Telescope Discovers a Disk Fueling a Possible Black Hole*, web site. URL: `http://hubblesite.org/newscenter/newsdesk/archive/releases/1992/27/`, 1992.

[82] D. Pandel, *Bestimmung von Wasser- und Detektorparametern und Rekonstruktion von Myonen bis 100 TeV mit dem Baikal-Neutrinoteleskop NT-72*, Diplom thesis, Humboldt-Universität zu Berlin, in German, 1996.

[83] J. R. Petit et al., *Climate and atmospheric history of the past 420,000 years from the Vostok ice core, Antarctica*, Nature **399** (1999), 429–436.

[84] P. B. Price, *Kinetics of Conversion of Air Bubbles to Air Hydrate Crystals in Antarctic Ice*, Science **267** (1995), 1802–1804.

[85] P. B. Price, K. Woschnagg, and D. Chirkin, *Age vs. depth of glacial ice at South Pole*, Geophysical Research Letters **27** (2000), no. 14, 2129–2132.

[86] P. B. Price et al., *Temperature profile for glacial ice at the South Pole: Implications for life in a nearby subglacial lake*, Proceedings of the National Academy of Sciences of the United States of Amerika **99** (2002), no. 12, 7844–7847.

[87] K. Rawlins, *Measuring the composition of Cosmic Rays with the SPASE and AMANDA detectors*, Ph.D. thesis, University of Wisconsin, Madison, 2001.

[88] N. Schmitz, *Neutrinophysik*, Teubner Studienbücher Stuttgart, 1997 (in German).

[89] P. Schneider, *Einführung in die Extragalaktische Astronomie*, (2002) (in German), chapter 5; lecture available from `http://www.astro.uni-bonn.de/~peter/Intro.html`.

[90] C. Spiering, *Das Neutrino-Teleskop im ewigen Eis*, Physik in unserer Zeit (2000), 56–62 (in German).

[91] C. Spiering, *Neutrino Astrophysics in the Cold: Amanda, Baikal and IceCube*, (2004), Talk given at the Nobel Symposium on Neutrino Physics, Haga Slott, Sweden, e-print `arXiv:astro-ph/0503122`.

[92] P. Steffen et al., *Sieglinde*, web site. URL `http://amanda.wisc.edu/software/sieglinde/`.

[93] P. Steffen, private communication.

[94] P. Steffen, *F2000: A standard AMANDA offline event format*, web site. URL `http://www-zeuthen.desy.de/~steffenp/f2000/`.

[95] T. J. Summer, *Experimental Searches for Dark Matter*, Living Reviews in Relativity (2002), available from URL: `http://www.livingreviews.org`.

[96] I. Tamm, *Radiation Emitted by Uniformly Moving Electrons*, Journal of Physics **1** (1939), no. 5-6, 439–454.

[97] M. Tegmark, *Cosmological neutrino bounds for non-cosmologists*, in "Neutrino Physics", Proceedings of Nobel Symposium 129 (2005), e-print `arXiv:hep-ph/0503257`.

[98] K. Woschnagg for the AMANDA collaboration, *New results from the Antarctic Muon And Neutrino Detector Array*, Nuclear Physics B (Proceedings Supplement: Proceedings of the XXIst International Conference on Neutrino Physics and Astrophysics, Paris, June 14-19, 2004) (2004), e-print `arXiv:astro-ph/0504380`.

[99] G. Walker, R. Atkins, and D. Kieda, *Evidence for New Unidentified TeV γ-ray Sources from Angularly-Correlated Hot-Spots Observed by Independent TeV γ-ray Sky Surveys*, e-print `arXiv:astro-ph/0409003`, 2004.

[100] E. Waxman and J. Bahcall, *High energy neutrinos from astrophysical sources: An upper bound*, Physical Review D **59** (1998), 023002, e-print `arXiv:hep-ph/9807282`.

[101] K. Woschnagg, *Review of Ice Models*, talk given at the AMANDA collaboration meeting in Madison. available from `http://amanda.berkeley.edu/kurt/ice2000/`, 2001.

[102] K. Woschnagg, *Optical Properties of Ice (in AMANDA and IceCube)*, web site. URL `http://amanda.berkeley.edu/kurt/ice2000/`, 2004.

[103] K. Woschnagg and others (the AMANDA collaboration), *Optical Properties of Deep Glacial Ice at South Pole*, Journal of Geophysical Research, to be published (2005).

[104] S. You, G. S. Yun, and P. M. Bellan, *Dynamic and Stagnating Plasma Flow Leading to Magnetic-Flux-Tube Collimation*, Physical Review Letters **95** (2005), 045002, see also Physical Review Focus **16**, story 4, available from `http://focus.aps.org/story/v16/st4`.

[105] K. Yurkewicz, *Extreme Neutrinos*, Symmetry **01** (2004), available from `http://www.symmetrymagazine.org/cms/?pid=1000014`.